Available online at www.sciencedirect.com
ScienceDirect
Trans. Nonferrous Met. Soc. China 33(2023) 231−253
Transactions of Nonferrous Metals Society of China
www.tnmsc.cn

Deep exploration of W−Sn and Cu polymetallic deposits in middle Qin−Hang metallogenic belt, South China

Qian-wei DAI, Dan DUAN, Biao LIU, Qian-hong WU,
Jia-bin YAN, Hua KONG, She-fa CHEN, Qi ZONG, Yu-yu TANG

Key Laboratory of Metallogenic Prediction of Nonferrous Metals and Geological Environment Monitoring, Ministry of Education, School of Geosciences and Info-Physics, Central South University, Changsha 410083, China

Received 30 September 2021; accepted 24 January 2022

Abstract: Field and microscopic structural investigations, trace element and C–O isotopic analyses of calcite, zircon U−Pb dating of dikes, and wide-field electromagnetic sounding are conjointly conducted in the middle part of the Qin−Hang metallogenic belt to decipher the spatial−temporal evolution and genetic relationship of structure−magma-mineralization. The data reveal four deformation events: D1 is a W-to-E-thrusting event; D2 is characterized by SE-to-NW thrusting; D3 is a NW−SE-oriented extensional event accompanied by large-scale magma intrusion and W–Sn and Cu–Pb–Zn mineralization; D4 is a dextral strike−slip event after mineralization. Two stages of calcite are identified during D_3 and Stage II calcite is characterized by LREE-enriched REE patterns, with low $\delta^{18}O_{SMOW}$ (from 9.78‰ to 12.3‰), identical to those of calcite in the deposits, confirming that they are closely related to mineralization. Wide-field electromagnetic profiles further display the geometric characteristics of structures, granitic plutons, and orebodies from shallow to deep (~5 km) level. It is believed that some giant concealed W−Sn and Cu−Pb−Zn orebodies are developed in the contact zones between plutons and limestone at a depth of 1.5−4 km. It is reasonable to suggest that this method is feasible for the study on the deep exploration of W−Sn and Cu−Pb−Zn polymetallic deposits.
Key words: fault; granitic pluton; calcite; REE pattern; wide-field electromagnetic sounding

1 Introduction

The Qin−Hang metallogenic belt is the suture zone between the Yangtze and Cathaysia blocks [1] (Fig. 1(a)), and several giant W–Sn and Cu–Pb–Zn deposits, such as the Shizhuyuan, Xianghualing, Baoshan, Huangshaping, Tongshanling, Shuikoushan, and Yaogangxian deposits, are concentrated in its middle part, and account for >30% of tungsten production in the world [1−3] (Fig. 1(b)). The W−Sn and Cu−Pb−Zn deposits were mainly formed in the Middle and Late Jurassic (150−165 Ma) and related to the small contemporaneous granitic intrusions or felsic dykes. They are dominated by skarn type and quartz vein type of deposits and are distributed along or adjacent to the N- to NNE-trending regional faults [1,2] (Fig. 2). The skarn type orebodies occur in the contact zones between the granitic plutons and limestone or dolomite, and quartz vein type orebodies are filled in the fractures within sandstone or granitoid [3,4]. After nearly 50 years of mining, shallow mineral resources at a depth of 0−1.5 km are gradually reduced, and the deep exploration (1.5−5 km) has become a scientific frontier and key issue for the study of mineral deposits. However, due to the superposition of multiple tectonic events, magmatic activities and hydrothermal alteration, there is no effective method to accurately identify and locate deep orebodies.

The artificial reflection seismic profile in this

Corresponding author: Biao LIU, Tel: +86-13207318788, E-mall: Biaoliu@csu.edu.cn
DOI: 10.1016/S1003-6326(22)66103-X

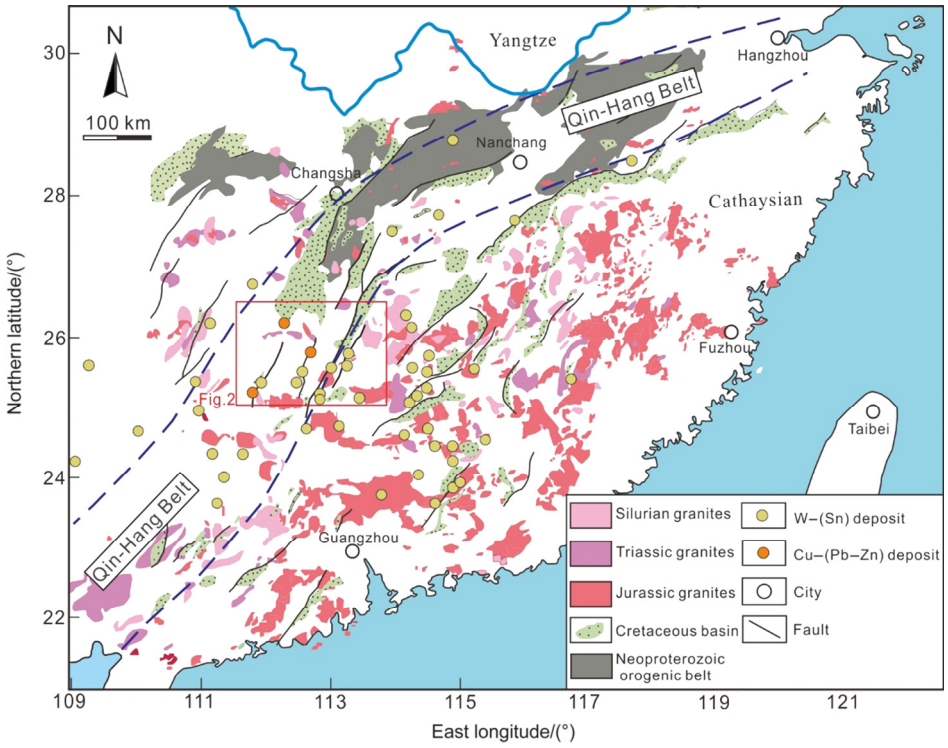

Fig. 1 Geology and distribution of major W−Sn polymetallic deposits in South China (modified from MAO et al [1])

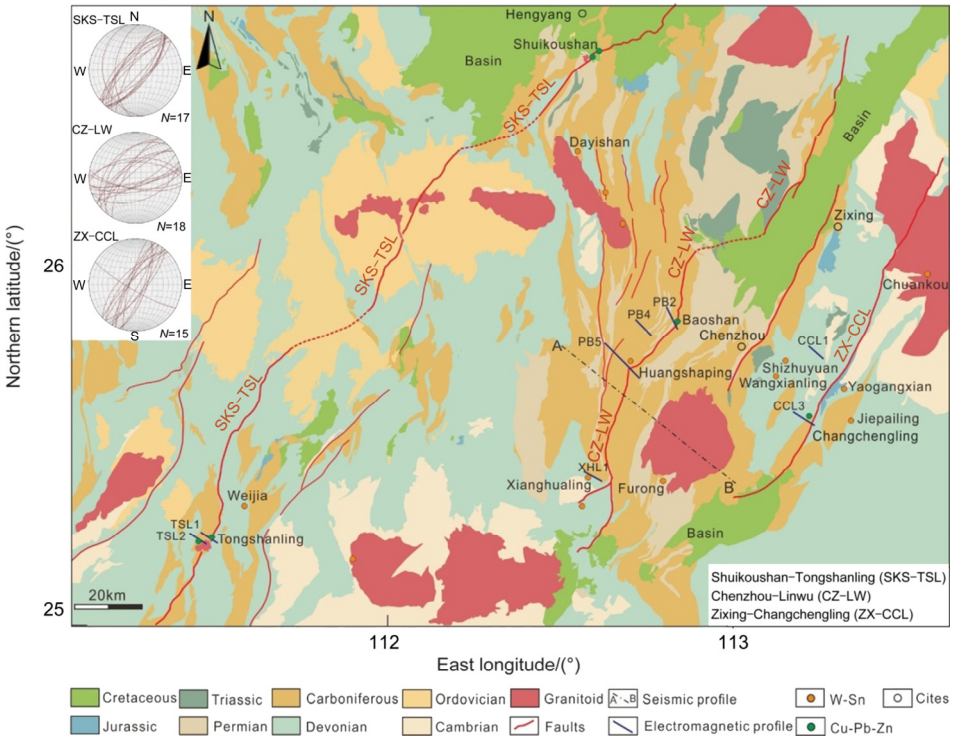

Fig. 2 Simplified geological map of middle Qin−Hang metallogenic belt, South China, showing Late Mesozoic granitoids, major W−Sn and Cu−Pb−Zn deposits

region reveals the crustal structures, mohorovicic discontinuity (~38 km) and faults at different depths [5] (Fig. 3). Some obvious low-velocity anomalies are revealed deep in the regional faults, which may be the result of the upwelling of asthenosphere [5]. This triggered a large-scale Jurassic granitic magmatic activity and W−Sn and Cu−Pb−Zn mineralization, implying an extensional tectonic

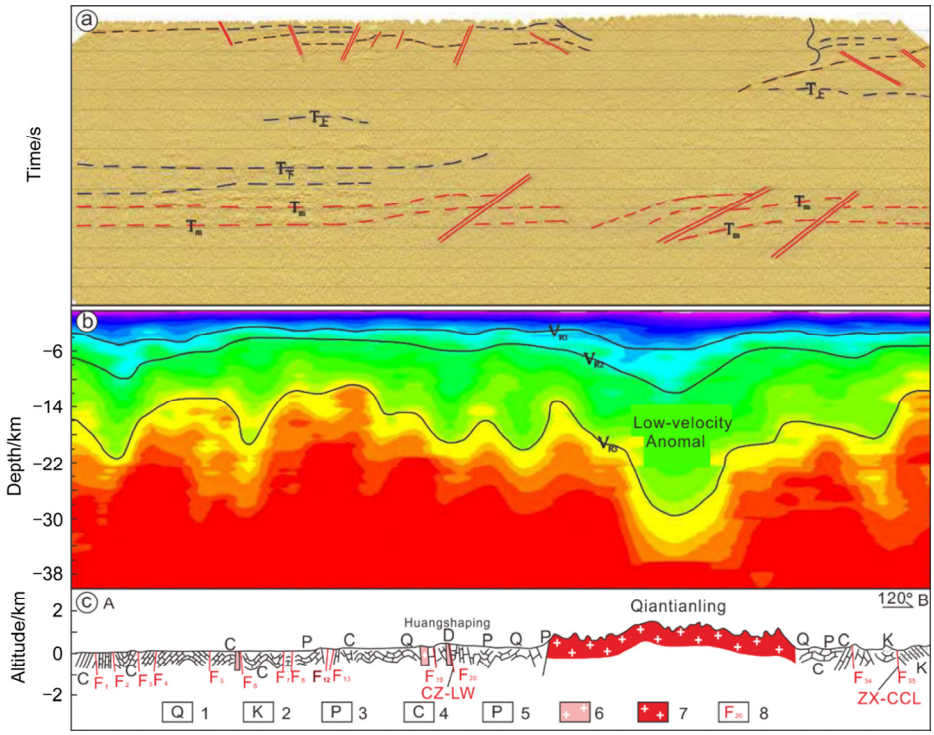

Fig. 3 Artificial seismic profile from 0 to 20 s in Qitianling profile (a); Inversion velocity of reflected seismic wave in Qitianling profile (b); Geological cross section A−B, with location shown in Fig. 2 (modified from LI et al [5])

setting [6]. The large-scale thrust faults with a small dip angle developed in the lower crust (~28 km) may be the result of the Triassic collision that is the opposite of the extensional setting [5]. However, the high-angle faults (<10 km) in the upper crust may be the main intrusion channels of granitic plutons, which is consistent with the faults, dykes, and W−Sn and Cu−Pb−Zn deposits in the shallow level (<1.5 km) (Fig. 3). The W−Sn ore-forming granites in the Qin−Hang metallogenic belt are characterized by A-type granitic rocks that are originated from partial melting of metamorphic basement rocks with a certain percentage of mantle-derived materials [6,7], implying a significant Mesozoic extensional regime in South China. In addition, a series of regional normal faults, grabens, and bimodal volcanic rocks, NW−SE oriented magnetic fabrics in the granitic plutons formed in Jurassic are also revealed on the surface and shallow crust (<1.5 km), which further confirms that the extensional event during Jurassic was closely related to the large-scale W−Sn and Cu−Pb−Zn mineralization [7,8]. However, the detailed characteristics of structures, granitic intrusions, hydrothermal alteration, and the W−Sn and Cu−Pb−Zn orebodies at a depth of 1.5−5 km are controversial, although they are critical for the study on the genetic relationship of structure−magma-mineralization and deep exploration.

In this study, to unveil the spatiotemporal evolution process of faults and W−Sn and Cu−Pb−Zn polymetallic mineralization in the middle Qin−Hang metallogenic belt, we have conducted field structural investigations, microscopic identification, geochemical analysis of calcite, chronology analysis of granitic dikes filling in the Shuikoushan−Tongshanling (SKS−TSL), Chenzhou−Linwu (CZ−LW) and Zixing−Chengchengling (ZX−CCL) faults. The REE and C−O isotopic compositions of calcite in faults and W−Sn and Cu−Pb−Zn deposits are compared to constrain the origin of fluids (<1.5 km) and to trace deep magma hydrothermal activity. The wide-field electromagnetic profiles are also used to reveal detailed characteristics of structures and granitic plutons at a depth of 1.5−5 km and to establish a new method for accurately identifying the W−Sn and Cu−Pb−Zn orebodies related to the magmatic hydrothermal fluids.

2 Geological background

The Yangtze and Cathaysia blocks experienced multiple stages of convergent and divergent

deformation in the Proterozoic, and the Qin−Hang metallogenic belt was finally formed in the early Paleozoic [9,10]. It has undergone two stages of tectonic events (Indosinian and Yanshanian) during the Mesozoic. The Indosinian tectonic event was the result of collision among the Sibumasu, Indo-china and South China Blocks during the late Permian (262−267 Ma [11]). The strong compressional deformation with folding and thrusting occurred in the South China Block and some granitic plutons were emplaced in the syn-collision or post-collision period [12]. The tectonic event in the Early Jurassic is characterized by some reverse faults due to the subduction of the Pacific plate with partial melting of asthenospheric mantle [7,13]. In the Middle Jurassic, the break-off or roll-back of subducting slab resulted in a release of compressional stresses and shift from compressional to extensional deformation [14]. The upwelling mantle triggered the remelting of the lower crust with large-scale granite activity and W−Sn and Cu−Pb−Zn mineralization in the South China [1,15].

The granites in the middle Qin−Hang metallogenic belt can be subdivided into the Silurian, Permian to Triassic, and Jurassic granites. The emplacement ages of Silurian granites are concentrated between 414 and 436 Ma, with the characteristics of S-type granites [16]. The emplacement ages of the Permian to Triassic granites are mainly 250−260 Ma and 220−230 Ma, with the characteristics of S-type or I-type granites [12,17]. The Jurassic granites are mainly composed of granodiorite, and biotite to muscovite granite: the former has an emplacement age of 155−165 Ma, with the characteristics of Type I granites, mainly forming Cu−Pb−Zn deposits [18]; the latter is mainly concentrated in 155−165 Ma, with the characteristics of A-type granite, and is closely related to W−Sn mineralization [2,6]. In the east of CZ−LW fault, a large area of Jurassic granite is exposed on the surface, while a few small rock masses and dykes are distributed in the west [19].

The middle Qin−Hang metallogenic belt has widely distributed W−Sn and Cu−Pb−Zn deposits [1,2,3,20], which can be divided into the skarn, greisen, and quartz vein types [21]. The quartz vein type orebodies mainly fill in the joints and fractures within the pre-Paleozoic metamorphic sandstones, early Devonian clastic rocks, and ancient granite [22], and the greisen type orebodies are developed in contact zones of plutons [23]. The skarn-type orebodies mainly occur in the contact zones between the Upper Devonian−Carboniferous limestone and plutons [3,21]. In the quartz vein type system, from shallow to deep level, the width of the quartz veins gradually increases (a few centimeters to a few meters) and metallogenic metals change from W−Sn to Nb−Ta, which is proposed as a “five-storey” model [23]. Some stratiform or lenticular concealed greisen type and quartz vein type (15−45 cm) W−Sn orebodies are revealed by the scientific drilling (NLSD-1, 3 km) at a depth of 1680 m in the granitic plutons [24], denoting another metallogenic system in the deep (>1.5 km). In the skarn type system, the orebodies are controlled by the shape of the contact zones or faults, and metallogenic metals change from Ag−Pb−Zn to Cu−W−Sn−Mo [3], such as the Baoshan Cu polymetallic and Shizhuyuan W–Sn polymetallic deposits.

3 Samples and analytical methods

3.1 Sample collection and preparation

The granitic dike and calcite samples were taken from the outcrop along the SKS−TSL, CZ−LW and CHL−ZX faults, and ore samples were collected from the underground mining tunnels of the Baoshan Cu−Pb−Zn deposit, Tongshanling Cu−Pb−Zn deposit, Weijia W deposit and Changchengling Rb−Pb−Zn deposit. In addition, some calcite samples in the CZ−LW fault were collected from the scientific drilling (ZK16508) at a depth of 1700 m and the detailed sample information is given in Table 1. Thin sections with a thickness of 60−80 μm were cut from calcite samples for laser ablation−inductively coupled plasma−mass spectroscopy (LA−ICP−MS) analyses.

3.2 Wide-field electromagnetic sounding

The wide-field electromagnetic sounding is improved from the traditional CSAMT and MELOS methods [25]. It is measured in single or multiple components by the artificial field source emission current and the apparent resistivity is computed by the wholesale methods. A total of 16 wide-field electromagnetic profiles were implemented in the study area, of which there are 2 profiles across the SKS−TSL faults, 8 profiles across the CZ−LW

Table 1 Sample information of granitoids and calcite in middle Qin−Hang metallogenic belt

Sample No.	Location	Stage of calcite	Mineral assemblage
201225-17S1	SKS−TSL fault	−	Fine-grained granite
ZK701	SKS−TSL fault	−	Quartz porphyry
20200824-7s1	Tongshanling deposit	−	Granodiorite
ZK902-245	Weijia deposit	−	Granite porphyry
0530-13S1	SKS−TSL fault	I	Calcite
825-8S2	SKS−TSL fault	II	Calcite + Hematite + Sericite
0530-1S1	SKS−TSL fault	II	Calcite + Hematite + Sericite
827-9S1	CZ−LW fault	I	Calcite
827-3s4	CZ−LW fault	II	Calcite + Hematite + Sericite
16508-534	CZ−LW fault	II	Calcite + Hematite + Sericite
829-8s1	ZX−CCL	I	Calcite
829-10S1	ZX−CC	I	Calcite
828-3s5	ZX−CC	II	Calcite + Hematite + Sericite
0602-5S2	Tongshanling deposit	I	Calcite + Diopside + Garnet
823-3s2	Tongshanling deposit	II	Calcite +Sulfide + Quartz
822-2S7-02	Weijia deposit	I	Calcite + Epidote + Chlorite
822-2S7-01	Weijia deposit	II	Calcite + Fluorite + Quartz

fault, and 3 profiles across the ZX−CCL fault. All exploration lines are perpendicular to the strike of three faults, as shown in Fig. 2. It adopts the E-Ex observation method, the AB distance is 1 km in length, and the space between receivers is greater than 13 km. The length of the emission dipole moment is 1.5 km, the transmitting power is 180 kW, and the maximum current is 130 A. In addition, a mapping analysis with a line spacing of 100 m and a point spacing of 50 m has also been carried out in the Baoshan Cu polymetallic deposit. The data processing is based on the conductivity of the rock by removing the flying spots of the original data, static correction, and other methods. Qualitative analysis is completed by combining the original data "frequency−apparent resistivity" curve [25].

3.3 CL images and U–Pb dating of zircon

Zircon cathodoluminescence (CL) images were taken at the Beijing Zhongke Kuangyan Test Technology Co. Ltd., using an analytical scanning electron microscope (Tescan MIRA 3) connected to a GATAN MINICL system. In situ zircon U–Pb dating, and trace element measurements were conducted using LA−ICP−MS in the Key Laboratory of Metallogenic Prediction of Nonferrous Metals and Geological Environment Monitoring, Central South University, Changsha, China. The spot size and frequency of the laser were set to be 32 μm and 5 Hz, respectively, in this study. Zircon 91500 and glass NIST610 were used as external standards for U–Pb dating and trace element calibration, respectively. Data reduction was performed by using GLITTER 4.4.4 developed by GEMOC and according to the standard method, and the Ca content of calcite was analyzed by EPMA [26].

3.4 Lu–Hf analysis of zircon

In-situ analysis of zircon Lu−Hf isotope compositions was carried out by using laser ablation−multi-collector−inductively coupled plasma−mass spectroscopy (LA−MC−ICP−MS) in the Beijing Geoanalysis Co., Ltd. (China). The ablation spots for Hf isotope analyses were situated over or close to the U–Pb age analysis positions on each zircon grain. The ablation spot size is 45 μm, the repetition rate is 10 Hz, and the energy density of 5.3 J/cm^2. The standard zircons Plešovice was measured to correct Hf isotopic values, which was analyzed twice every 10 samples. Detailed

operating conditions and analytical methods for LA−ICP−MS and LA−MC−ICP−MS are described by GRIFFIN et al [26].

3.5 LA−ICP−MS analysis of calcite

In situ trace element analyses of calcite were also performed using LA−ICP−MS in the Key Laboratory of Metallogenic Prediction of Nonferrous Metals and Geological Environment Monitoring, Central South University, Changsha, China. Individual calcite grains were measured using a Teledyne Photon Machines Analyte HE Excimer 193 nm laser ablation system, coupled to an Analytik Jena Plasma Quant MS Ellite ICPMS at the Key Laboratory of Metallogenic Prediction of Nonferrous Metals and Geological Environment Monitor of Ministry of Education, Central South University, Changsha, China. The selected thin sections were cleaned and placed into the HelEx II chamfer cell of the laser. The samples were placed in a sealed ablation cell that was constantly flushed with a mixture of high purity Ar (13.5 L/min) and He gases (1.1 L/min). Spot sizes were 35 μm. The laser repetition rate was typically 5 Hz and laser beam energy at the sample was maintained around 2.0 J/cm^2. NIST610, BHVO, GSE-1 and BIR-1G were used as external standard for analyses, and NIST SRM610 was used as the system monitoring sample. Data reduction was performed by using GLITTER 4.4.4 developed by GEMOC and according to the standard method, and the Ca content of calcite was analyzed by EPMA [26]. Results for all measured trace elements were in good agreement with published standard materials.

3.6 C−O isotope analysis of calcite

The carbon and oxygen isotope composition analysis of calcite was conducted in the Laboratory of Beijing Institute of Geology of Nuclear Industry (China). The analysis systems consist of a Thermo Finnigan Gas Bench II equipped with a CTC Combi-Pal autosampler and linked to a Finnigan 253puls mass spectrometer. Calcite micro-samples are loaded manually into 12 mL round-bottomed borosilicate exetainers and sealed using butyl rubber septa. 26 exetainers including 18 aliquots of four national standards (GBW04405, GBW04406, GBW04416 and GBW04417) are routinely loaded for one run. The exetainers are automatically flushed with Grade 5 He by penetrating the septa using a double-hole needle at a flow rate of 100 mL/min. Afterwards, 4−6 drops of phosphoric acid were deposited in each exetainer. The exetainers were placed into an aluminum tray kept at 72 ℃ for 4 h to calcite. Subsequently, the sample gas was introduced ten times into the mass spectrometer, by sampling through the standard 100 μL sample loop; CO_2 was separated from other components using a gas chromatographic column (Poraplot Q with fused-silica tubing, 25 m × 0.32 mm, Thermo Fisher Scientific) heated to 70 ℃, and the peak corresponding to this CO_2 was then passed via an open split into the mass spectrometer. The external precision calculated over 18 standards per run was typically 0.1‰ for $\delta^{13}C$ and $\delta^{18}O$. The formula used for conversion between PDB and SMOW is as follows: $\delta^{18}O_{(V\text{-}PDB)}=(\delta^{18}O_{(V\text{-}SMOW)}-30.91)/1.0309$ [27].

4 Analytical results

4.1 Deformation history and structural characteristics

4.1.1 Compressional deformation (D_1 and D_2)

Two compressional deformation events (D_1 and D_2) occurred in the study area. In D_1, a series of upright and inclined folds were developed in the Devonian, Carboniferous, and Permian strata (Figs. 4(a, b)). Most folds trend N−S to NNE−SSW, and have symmetric and asymmetric geometry (Figs. 4(a, b)). Compaction cleavages are widely observed, and some regional reverse faults are also identified (Figs. 4(e−f)). These bedding-parallel cleavages strike nearly N−S to NNE−SSW with subvertical dips and are developed in zones with a width of several meters to tens of meters (Figs. 4(c, d)). Sericite and calcite in limestone are aligned in a N−S orientation (Fig. 4(e)). The three most significant faults are the SKS−TSL, CZ−LW and ZX−CCL faults from west to east that are closely related to magmatic activity and mineralization (Fig. 2).

The SKS−TSL fault extends for more than 150 km. It trends NE and dips 80° to the NW (Figs. 2 and 4(f)). The ZX−CCL fault, with a length of more than 100 km, trends NE and dips 80° to the NE (Fig. 2). However, the strike of the CZ−LW fault varies greatly, from NNE, N−S to NNW and displays an S shape in the Baoshan−Huangshaping

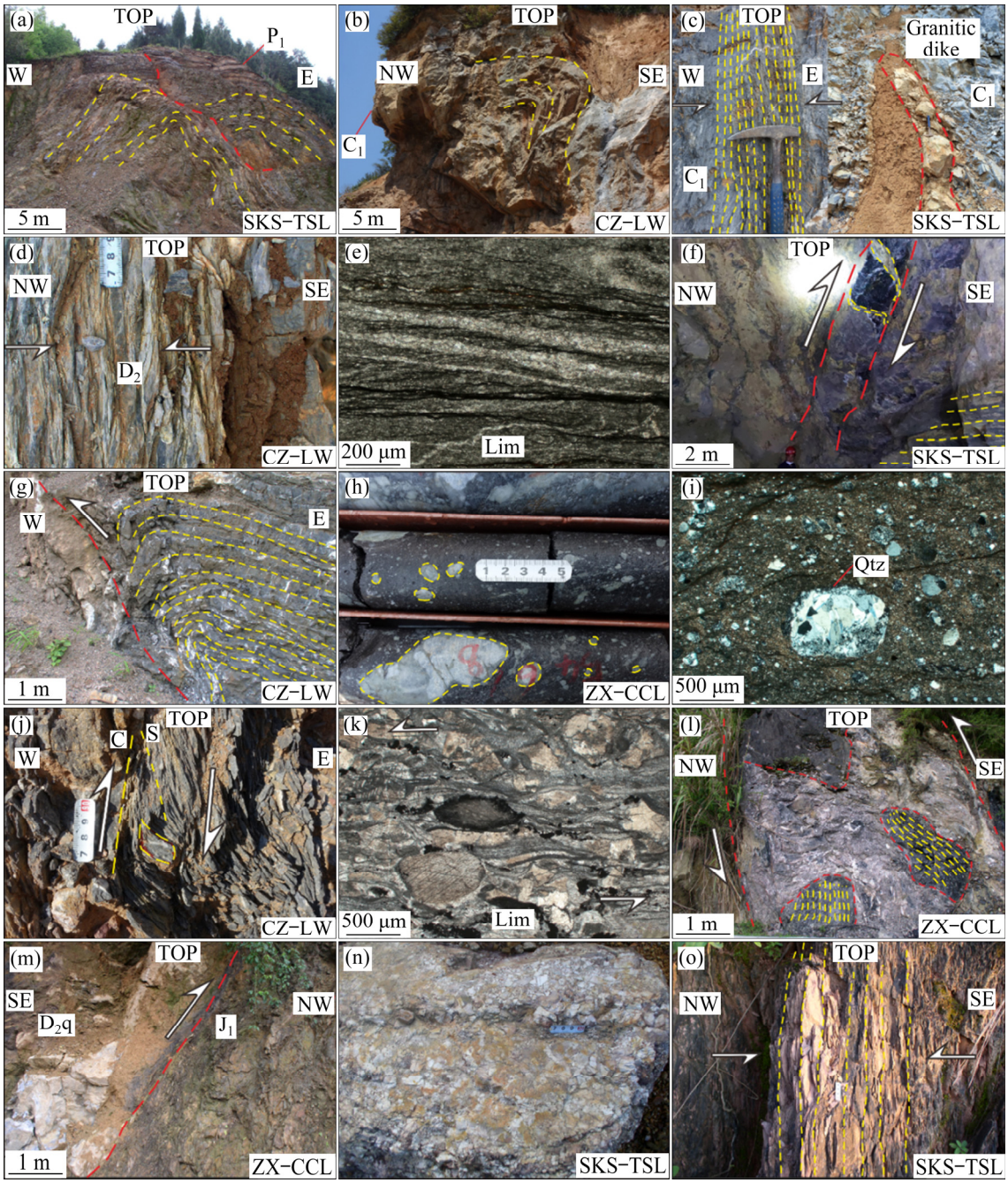

Fig. 4 Photographs and photomicrographs showing compressional structures in middle Qin−Hang metallogenic belt: (a, b) Folds developed in Carboniferous and Devonian limestone; (c−e) Bedding-parallel compaction cleavages; (f−i) Reverse faults and fault breccia in SKS−TSL, CZ−LW and ZX−CCL faults; (j) S−C fabrics indicating top to east thrusting direction; (k) Weak ductile deformation in CZ−LW fault; (l) Fault breccias containing cleavages in ZX−CCL fault; (m) Devonian limestone thrusting onto Lower Jurassic strata; (n) Angular fault breccias in Lower Jurassic strata; (o) Subvertical cleavage in Lower Jurassic strata

region (Figs. 2 and 4(g)). This fault dips to the NW in the Baoshan Cu−Pb−Zn deposit, but dips to the SE in the Huangshaping W−Sn deposit, with a dip angle of more than 60° (Fig. 2). Quartz grains in the faults are abraded, and siltstone and limestone are broken into small breccias (Figs. 4(g, i)). In addition, these faults are truncated by some small-scale but densely developed E- and WNW-trending cross-faults in some places (Fig. 4(a)).

Several small-scale NNE- to N-striking ductile shear zones are developed along the CZ−LW and ZX−CCL faults (Fig. 4(j)). They contain S−C fabrics and consist of mylonitized limestone and sandstone (Fig. 4(j)). S−C fabrics and σ-type

porphyroclasts suggest a top to the E or SE shearing (Figs. 4(j, k)). The early compressional structures described above indicate a kinematic regime dominated by nearly WNW−ESE shortening and local ductile shearing.

The rocks containing S_1 cleavages are broken into breccias by D_2 compressional deformation (Fig. 4(l)). Middle Devonian limestone (D_{2q}) thrusts onto Lower Jurassic rocks (J_1) along the ZX−CCL fault (Fig. 4(m)). In the SKS−TSL fault, the Early Jurassic formation (J_1) and Carboniferous formation are also characterized by conspicuous faulted contact with angular breccia at the bottom of Early Jurassic formation (J_1) (Fig. 4(n)). In addition, the Lower Jurassic rocks (J_1) are strongly deformed in some places, with a subvertical cleavage, as a result of D_2 compressional deformation (Fig. 4(o)). The D_2 compressional structures are derived from ESE−WNW shortening.

4.1.2 Extensional deformation (D_3)

D_3 normal faults trend NE and dip to SE, with a dip angle of 45°−65° (Figs. 5(a, b)). The relationship between the extensional joints in the hanging wall and the fault indicates a normal movement on the fault (Fig. 5(a)). Slickensides and slickenlines on the fault surface also indicate a normal faulting (Fig. 5(b)). The fault breccias developed in D_3 are angular, with various size (Figs. 5(c, d, e)). Most normal faults are reactivated from early reverse faults formed in compressional

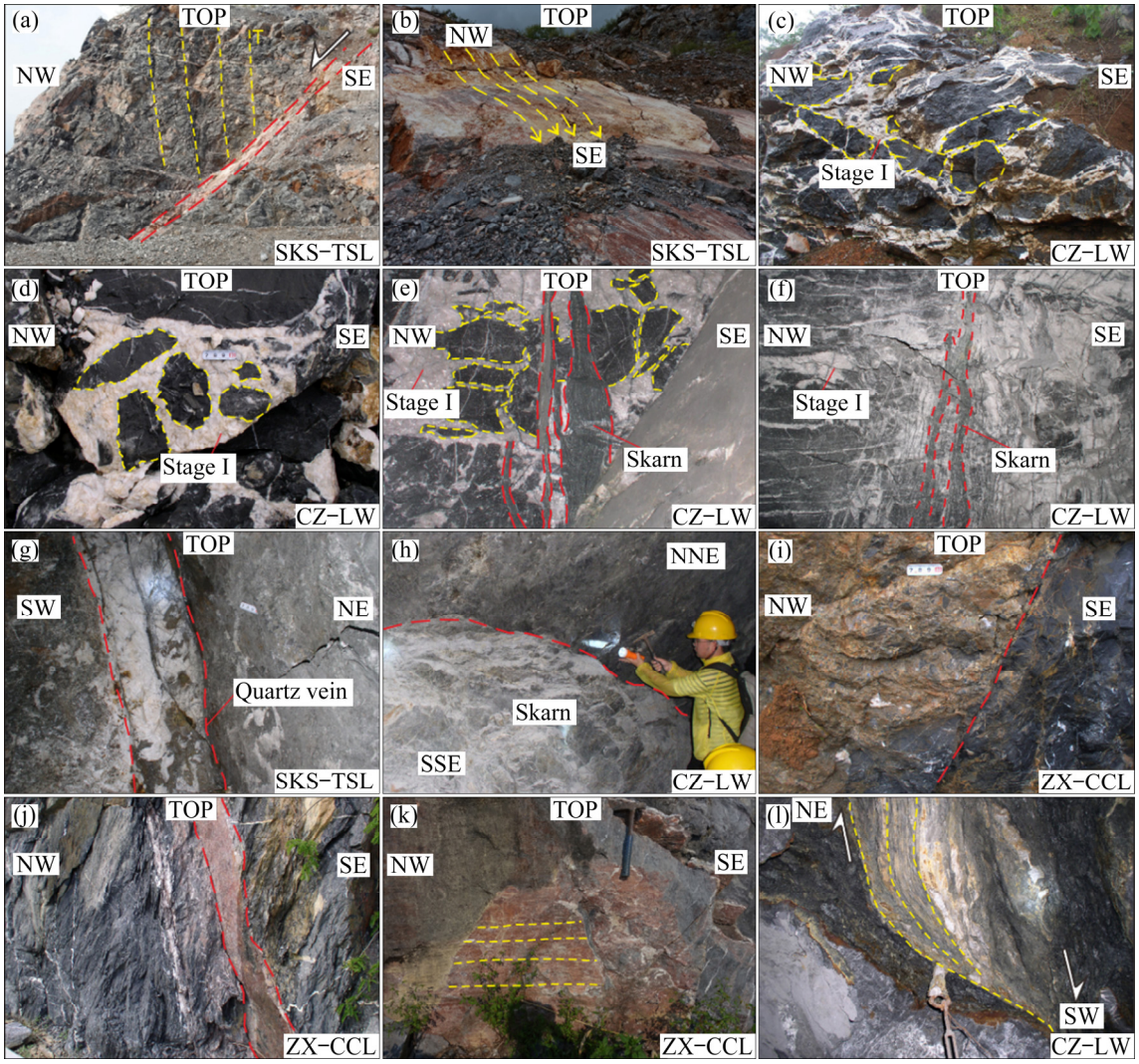

Fig. 5 Photographs showing extensional and strike−slip deformation characteristics in middle Qin−Hang metallogenic belt: (a, b) Normal fault developed in SKS−TSL fault; (c, d) Angular fault breccias cemented by Stage I calcite; (e, f) Skarn type veins cut through Stage I calcite in Xianghualing ore field; (g−i) Skarn type and quartz vein type veins filled in normal faults of SKS−TSL, CZ−LW and ZX−CCL faults; (j−l) Strike−slip deformation in CZ−LW and ZX−CCL faults

deformation, although their attitudes may have been changed (Fig. 2). Many granitic plutons and dykes were intruded during the extensional stage, and some of them were related to the N- to NNE-trending regional faults (Fig. 2). The granitic plutons can be divided into two types: I-type granodiorite (e.g., Tongshanling, Shuikoushan) is closely related to Cu−Pb−Zn mineralization; A-type or S-type granitic porphyry (e.g., Huangshaping, Weijia) is closely related to W−Sn mineralization.

In outcrops of regional faults and mining tunnels in the mineral deposits, a large number of calcite veins have been identified (Figs. 5(a, c−f)). Based on the cementation and cut-through relationships of calcite veins, calcite can be divided into two stages. Stage I calcite is coarse-grained and milky white, with no hydrothermal alteration of wall rocks (Figs. 5(c, d) and 6(a)). It cements fault breccias (Figs. 5(c−e)), but itself is also broken into breccias with an angular shape (Figs 6c, d). Stage II calcite is fine-grained and grease luster, with hematite mineralization and sericitization. Stage II calcite veins cut through or cement the Stage I calcite (Figs. 5(a) and 6(d−f)).

Both skarn and quartz vein orebodies are closely related to the normal faults (Figs. 5(g−i)). In the Tongshanling Cu polymetallic deposit, the quartz vein type orebodies are filled in the NW-striking secondary faults of the SKS−TSL fault (Fig. 5(g)). In the Baoshan Cu polymetallic deposit, the skarn orebodies are related to the NNE-striking SKS−TSL fault (Fig. 5(h)). In the Changchengling Rb−Pb−Zn deposit, the Pb−Zn mineralization is developed in the NE-striking ZX−CCL fault (Fig. 5(i)). The Stage I calcite is cut through by the W−Sn skarn veins in the Xianghualing ore field (Figs. 5(e, f)). In addition, two stages of calcite are also developed in the skarn and quartz vein ores (Figs. 6(g–i)), in which the Stage I calcite is intergrown with quartz, garnet, diopside and sulfide, while the Stage II calcite veins cut through garnet (Figs. 6(g, i)).

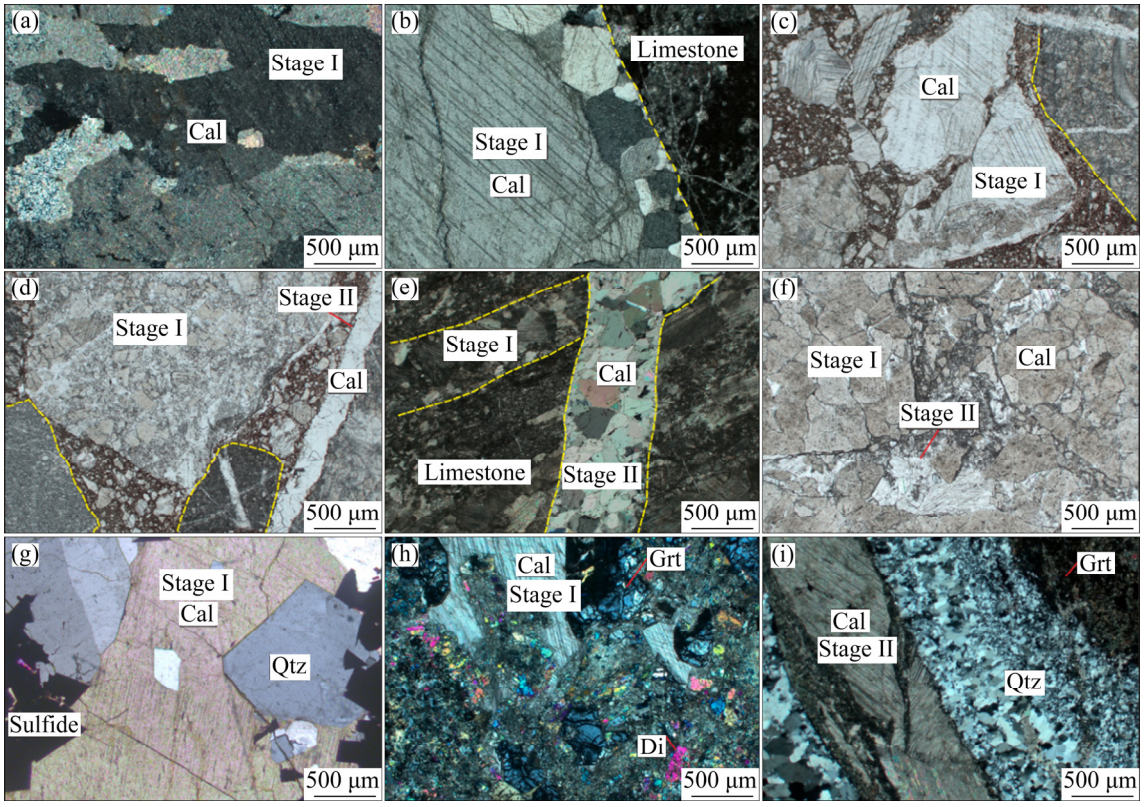

Fig. 6 Photomicrographs of calcite and calcite veins formed in different stages, with samples taken from fault zones and mineral deposits in middle Qin−Hang metallogenic belt: (a, b) Stage I coarse-grained calcite veins cutting through Carboniferous limestone; (c, d) Stage I calcite broken into angular breccias; (e) Stage II calcite vein cutting through Stage I calcite; (f) Stage II calcite cementing Stage I calcite breccias; (g) Calcite symbiotic with quartz and sulfide in Tongshanling Cu polymetallic deposit; (h) Calcite symbiotic with garnet and diopside in Weijia W polymetallic deposit; (i) Late calcite vein cutting through skarn orebody (Cal−Calcite; Qtz−Quartz; Grt−Granite)

4.1.3 Strike−slip deformation (D_4)

After large-scale magmatism and W−Sn and Cu−Pb−Zn mineralization in the Middle Jurassic, a phase of strike−slip deformation occurred (Figs. 5(j−l)). Subhorizontal slickenlines have been observed on the NE-trending fault planes, indicating a strike−slip deformation (Figs. 5(j−k)). However, the strike−slip displacement is not very large. Based on the discrimination of stratigraphic offset on both sides of the fault, the largest strike−slip displacement on the ZX−CCL and CZ−LW faults is about 300 m (Fig. 2), and it is only tens of meters on the SKS−TSL fault (Fig. 2). For this reason, the mineral deposits formed in the Middle Jurassic have been well preserved.

4.2 Wide-field electromagnetic profiles

Through static correction and two-dimensional constrained inversion, the discrimination ability of electromagnetic data in the deep level is improved, and the effective detection depth is up to 5 km (Fig. 7).

The wide-field electromagnetic inversion profiles reveal a heterogeneous distribution of apparent resistivity in the Baoshan Cu polymetallic deposit (Fig. 7(a)). Two abnormal high-resistance bodies (>7000 Ω·m) are identified under the CZ−LW fault (from 0 to −4000 m) and the F_{112} fault (Fig. 7(a), from −3500 to −4000 m), respectively, indicating two granitic intrusions. Some layered abnormal low resistance bodies (<200 Ω·m) are distributed in the shallow level (from +1000 to −2000 m), with opposite tendency in the northwest and southeast, corresponding to a surface syncline composed of carbonaceous shale and limestone (Fig. 7(a)). The relatively weak uplift and denudation of the core of the syncline developed in the Devonian and Carboniferous carbonate strata, which provided good surrounding rock conditions for the formation of large-scale skarn-type mineralization in the Jurassic. In the northwest, a vertical low-resistance belt (400−1000 Ω·m) cuts through the layered low-resistance body and connects the deep high-resistance body with the F_{112}

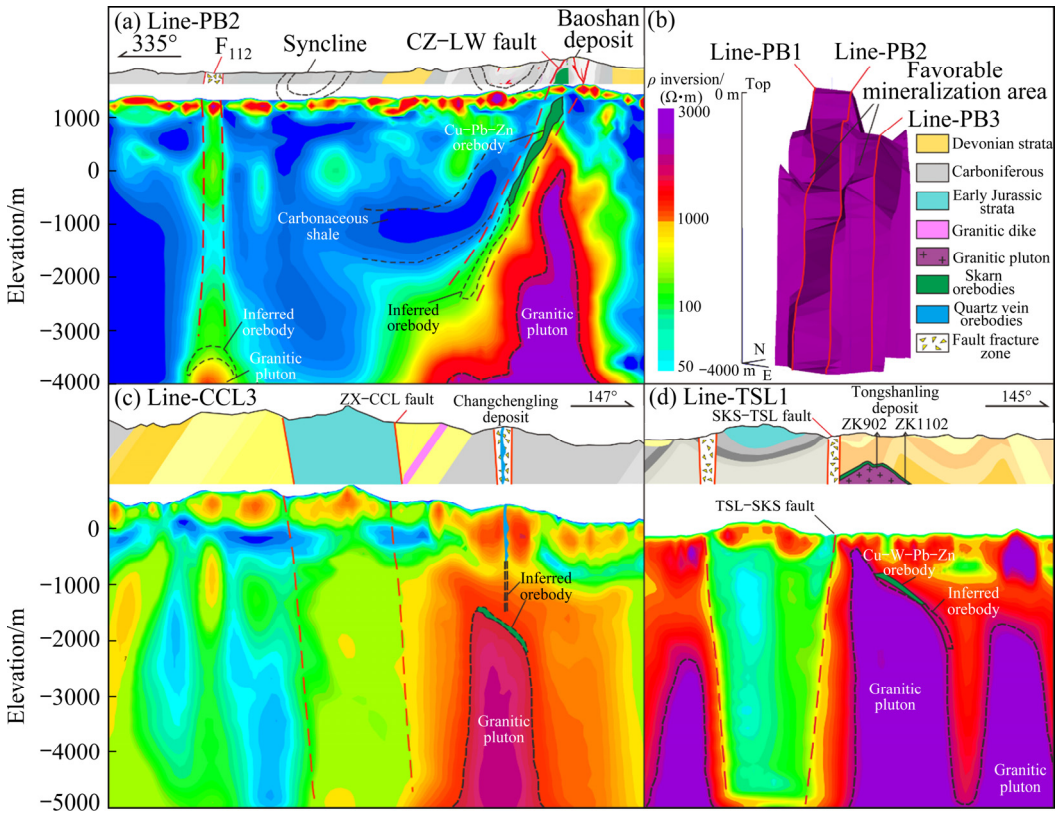

Fig. 7 Wide-field electromagnetic profiles and 3D model in middle Qin−Hang metallogenic belt (Profile locations are shown in Fig. 2): (a) Line-PB2 profile across CZ−LW fault and Baoshan Cu polymetallic deposit; (b) 3D model of abnormal high-resistance bodies (>7000 Ω·m) under Baoshan Cu polymetallic deposit; (c) Line-CCL3 profile across ZX−CCL fault and Changchengling Rb−Pb−Zn deposit; (d) Line-TSL1 profile across SKS−TSL fault and Tongshanling Cu polymetallic deposit

fault on the surface that may be caused by fault activity and hydrothermal alteration. In the southeast, a NW-dipping low-resistance belt (400−1000 Ω·m) with a dip angle of 60° is distributed between layered abnormal low resistance bodies and high resistance bodies and is coincident with the skarn type Cu−Pb−Zn orebodies and the CZ−LW fault. The low-resistance belt is stable and is extended to −2.5 km, suggesting a concealed skarn orebody.

The mapping analysis results and 3D modeling reveal the detailed three-dimensional feature of the abnormal high-resistance body (>7000 Ω·m) under the Baoshan Cu polymetallic deposit (Fig. 7(b)), which is confirmed to be a low-gravity anomaly by high-precision tunnel gravity measurement (unpublished). The highest point of the abnormal high-resistance body (>7000 Ω·m) is distributed between the Line-PB1 and Line-PB2 and some depression zones are also identified in Line-PB1 and Line-PB2 at the depth from −1000 to −1500 m, which are beneficial to skarn type mineralization.

Abnormal high-resistance body (>5000 Ω·m) is also identified in the Chengchengling Pb−Zn deposit, but there are no obvious apparent resistivity anomalies for the quartz vein type Pb−Zn orebodies in the shallow level (from +300 to −200 m), which may be related to the outcrop of surface rocks and the Quaternary coverage. An obvious vertical low-resistance anomaly (~400 Ω·m) is under the Lower Jurassic strata. It is inconsistent with the strata with a dip angle of 30°, and is more likely to be the result of the ZX−CCL fault. A possible skarn type orebody may occur in the contact zone between the high-resistance body and the Carboniferous limestone (Fig. 7(c)).

The wide-field electromagnetic inversion profiles in the Tongshanling Cu polymetallic deposit show similar features with those in the Baoshan and Changchengling deposits (Fig. 7(d)). The abnormal high-resistance body (>7000 Ω·m) has been confirmed by drilling (ZK902 and ZK1101) as granitic rock mass, and large-scale skarn Cu−W−Pb−Zn mineralization occurs in the contact zone (Fig. 7(d)). With the development of deep exploration, some concealed skarn type orebodies may be discovered in the deep contacts zone (from −1200 to −2500 m). The SKS−TSL fault is also characterized by the vertical low-resistance anomaly (~400 Ω·m) under the Lower Jurassic strata and cuts through the abnormal high-resistance bodies (Fig. 7(d)), implying the deformation after Jurassic mineralization.

4.3 Zircon U−Pb geochronology and Hf isotope

To further constrain the genetic relationship between granitic plutons and mineralization revealed by field observations and wide-field electromagnetic profiles, petrology, geochronology and Hf isotope of zircon in the SKS−TSL fault were analyzed. The analytical results of four samples, 75 highly reliable zircon U−Pb dates (concordance >90%), and corresponding Hf isotopic compositions are presented in Tables S1 and S2 in Supplementary information.

The granitic plutons and dikes intruded along three faults can be divided into four types: (1) fine-grained granitic dikes developed in compressional deformation (Figs. 8(a, b)); (2) quartz porphyry dikes filled in the NE- and NW-striking faults (Figs. 8(c, d)); (3) granodiorite related to Cu–Pb–Zn mineralization (Figs. 8(c, d)); (4) granitic porphyry related to the W–Sn mineralization. All the granitic plutons and dikes are massive, with granitic or porphyritic texture (Fig. 8). Major rock-forming minerals are quartz (40−60 vol.%), plagioclase (20−40 vol.%), biotite (0−20 vol.%), and minor muscovite (<5 vol.%). Phenocrysts are quartz and plagioclase, while the matrix is dominated by plagioclase, quartz, and biotite (Fig. 8). Zircon grains from granitic plutons and dikes in the SKS−TSL fault exhibit similar features and are mostly euhedral, with a length of 50−200 μm and aspect ratios of 1:1−3:1. CL imaging reveals that most of the zircon grains have internal oscillatory zonation, indicating a magmatic origin (Fig. 9) [28].

4.3.1 Triassic granitic dikes

The $^{206}Pb/^{238}U$ ages of 13 zircon grains from a granitic dike intruded in the compressional SKS−TSL fault are plotted on or close to the concordant curve, yielding a concordant age of (252.8±1.1) Ma (MSWD=0.97; Fig. 10(a)). The $^{176}Yb/^{177}Hf$ and $^{176}Lu/^{177}Hf$ ratios of 6 zircon grains range from 0.030476 to 0.067344 and from 0.001030 to 0.002197, respectively. The calculated initial $^{176}Hf/^{177}Hf$ ratios are 0.282308−0.282450, with $\varepsilon Hf(t)$ values from −10.79 to −5.87 (Fig. 11(a)) and T_{DMC} ages of 1651−1965 Ma (Table S2 in Supplementary information).

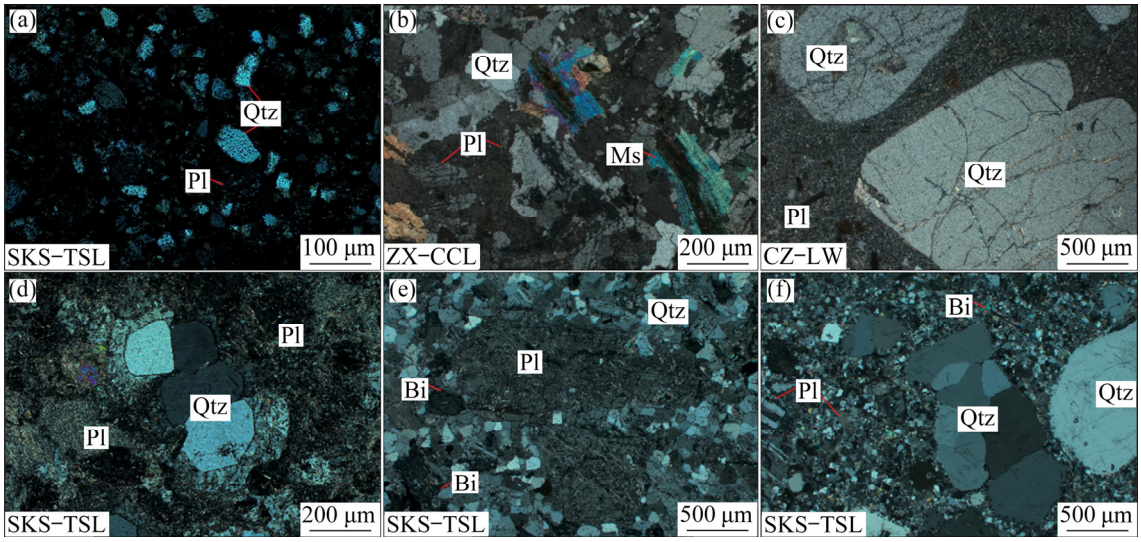

Fig. 8 Photomicrographs of granitoids in middle Qin−Hang metallogenic belt: (a) Triassic fine-grained granite in SKS−TSL fault; (b) Triassic two-mica granite in Changchengling Rb−Pb−Zn deposit; (c) Jurassic quartz porphyry in Baoshan Cu polymetallic deposit; (d) Jurassic quartz porphyry in SKS−TSL fault; (e) Jurassic granodiorite in Tongshanling Cu polymetallic deposit; (f) Jurassic granite porphyry in Weijia W deposit (Qtz−Quartz; Pl−Plagioclase; Ms−Muscovite; Bi−Biotite)

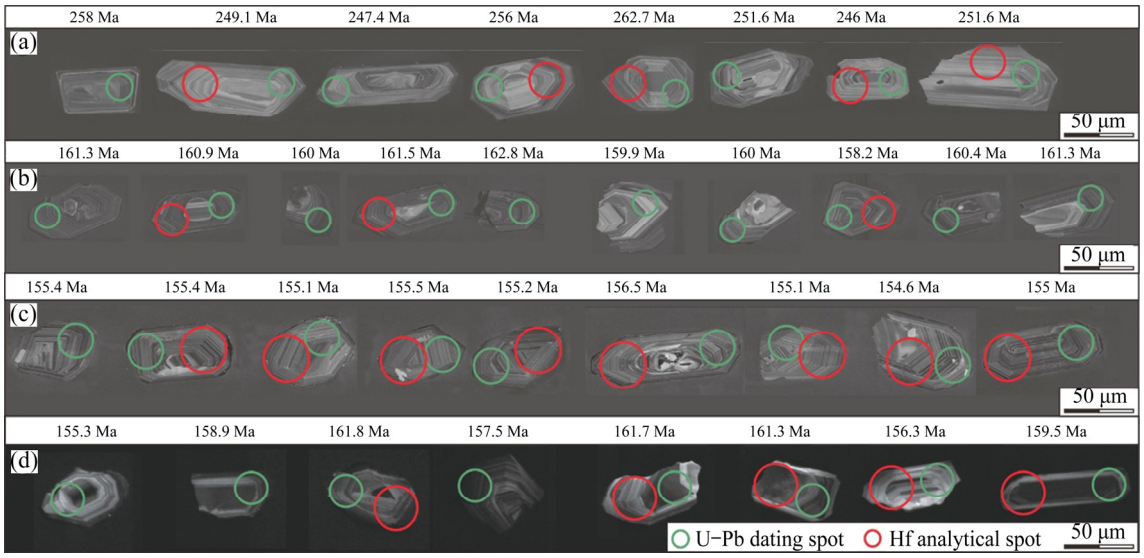

Fig. 9 CL images of zircon from granitoids in middle Qin−Hang metallogenic belt, with zircon grains: (a) Triassic fine-grained granite in SKS−TSL fault; (b) Jurassic quartz porphyry in SKS−TSL fault; (c) Jurassic granodiorite in Tongshanling Cu polymetallic deposit; (d) Jurassic granite porphyry in Weijia W deposit

4.3.2 Jurassic quartz porphyry dikes

The $^{206}Pb/^{238}U$ ages of 14 zircon grains from a quartz porphyry dike intruded in the extensional SKS−TSL fault are plotted on or close to the concordant curve, yielding a concordant age of (159.9±0.6) Ma (MSWD=0.32; Fig. 10(b)). The $^{176}Yb/^{177}Hf$ and $^{176}Lu/^{177}Hf$ ratios of 4 zircon grains from drill cores of ZK701 range in 0.029955−0.054982 and 0.001067−0.001922, respectively. The calculated initial $^{176}Hf/^{177}Hf$ ratios are 0.282527−0.282622, with $\varepsilon Hf(t)$ values ranging from −5.08 to −1.81 (Fig. 11(b)), and T_{DMC} ages of 1323−1533 Ma (Table S2 in Supplementary information).

4.3.3 Jurassic granodiorite

The $^{206}Pb/^{238}U$ ages of 14 zircon grains from granodiorite intruded in the extensional SKS−TSL fault are plotted on or close to the concordant curve, yielding a concordant age of (155.0±0.6) Ma, (MSWD=0.07; Fig. 10(c)). The $^{176}Yb/^{177}Hf$ and

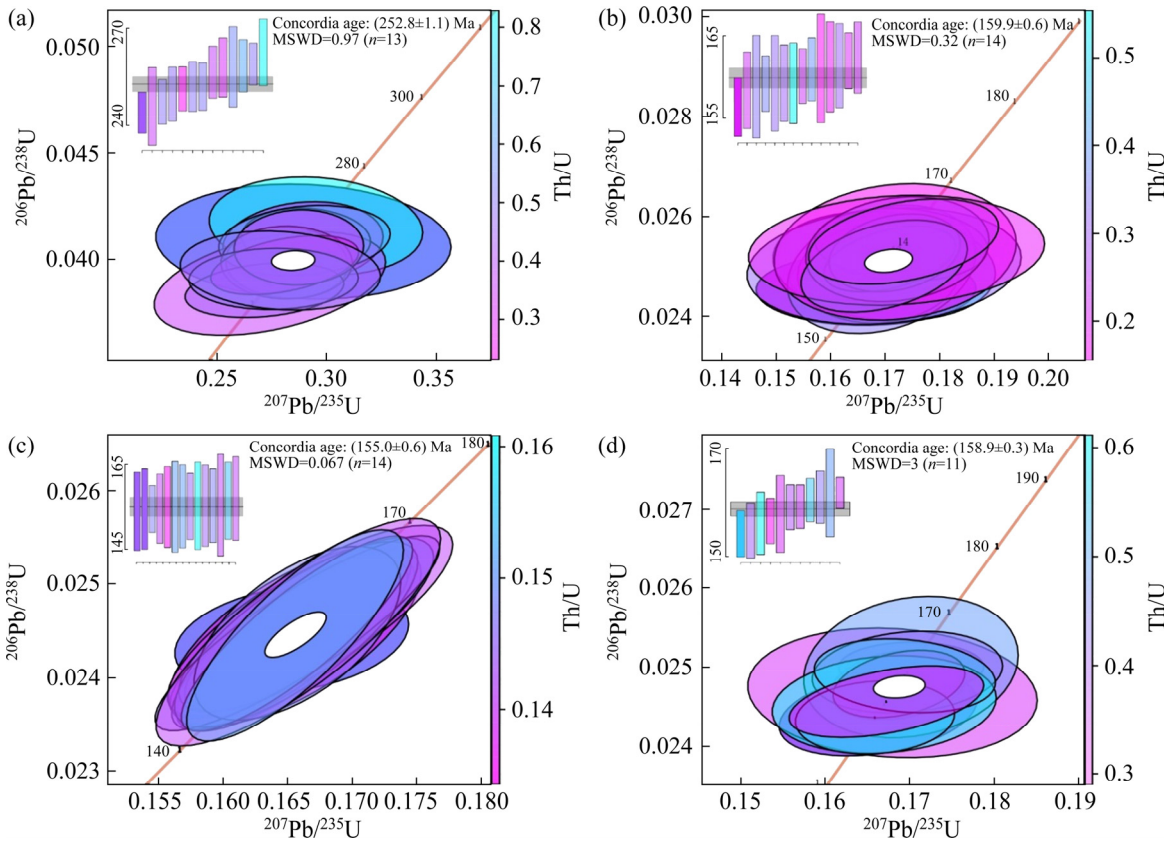

Fig. 10 Zircon U−Pb concordia and weighted mean age plots for granitoids in middle Qin−Hang metallogenic belt: (a) Triassic fine-grained granite in SKS−TSL fault; (b) Jurassic quartz porphyry in SKS−TSL fault; (c) Jurassic granodiorite in Tongshanling Cu polymetallic deposit; (d) Jurassic granite porphyry in Weijia W deposit

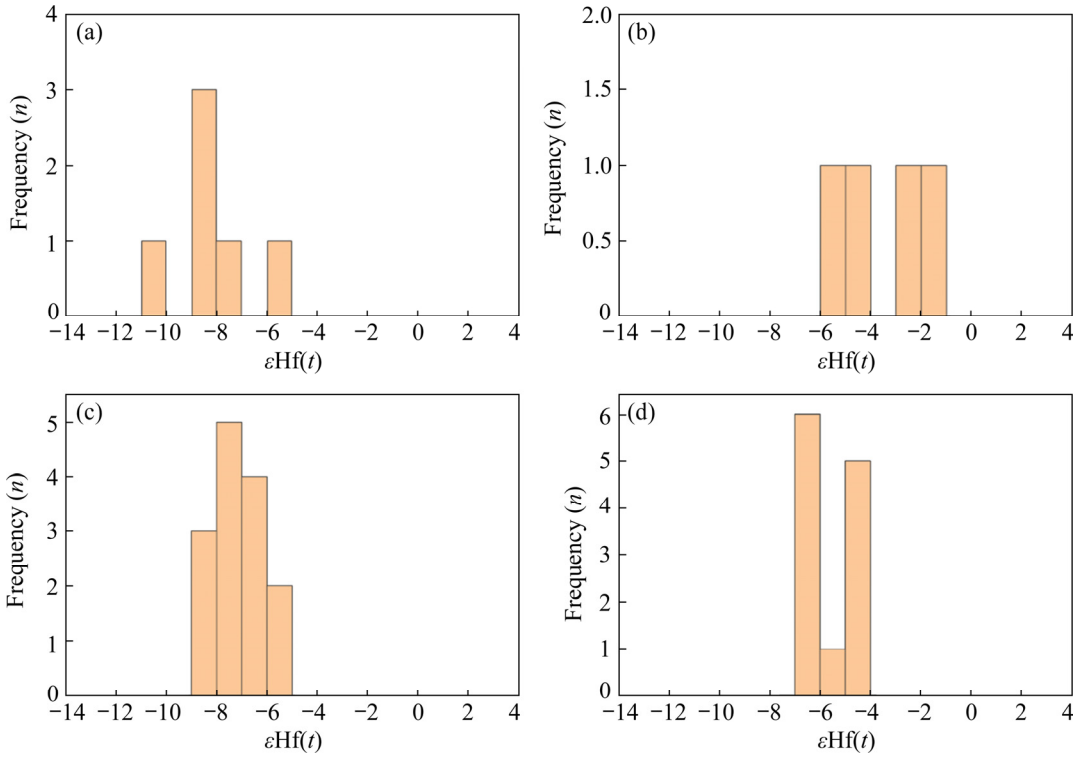

Fig. 11 Zircon $\varepsilon Hf(t)$ histograms of granitoids in middle Qin−Hang metallogenic belt: (a) Triassic fine-grained granite in SKS−TSL fault; (b) Jurassic quartz porphyry in SKS−TSL fault; (c) Jurassic granodiorite in Tongshanling Cu polymetallic deposit; (d) Jurassic granite porphyry in Weijia W deposit

$^{176}Lu/^{177}Hf$ ratios of 14 zircon grains from sample 20200824-7s1 range from 0.029348 to 0.041874 and from 0.001123 to 0.001856, respectively. The calculated initial $^{176}Hf/^{177}Hf$ ratios are 0.282388−0.282519, with $\varepsilon Hf(t)$ values ranging from −10.18 to −4.61 (Fig. 11(c)) and T_{DMC} ages of 1499−1850 Ma (Table S2 in Supplementary information).

4.3.4 Jurassic granite porphyry

The $^{206}Pb/^{238}U$ ages of 11 zircon grains from granite porphyry intruded in the extensional SKS−TSL fault are plotted on or close to the concordant curve, yielding a concordant age of (158.9±0.3) Ma (MSWD=3; Fig. 10(d)). The $^{176}Yb/^{177}Hf$ and $^{176}Lu/^{177}Hf$ ratios of 12 zircon grains from sample ZK902-245 are 0.020013−0.055455 and 0.000681−0.001785, respectively. The calculated initial $^{176}Hf/^{177}Hf$ ratios are 0.282482−0.282563, with $\varepsilon Hf(t)$ values ranging from −6.11 to −4.01 (Fig. 11(d)) and T_{DMC} ages of 1459−1636 Ma (Table S2 in Supplementary information).

4.4 Trace element compositions of calcite

A summary of trace element analytical results of calcite grains in the faults and mineral deposits is shown in Table S3 in Supplementary information, with detailed analytical data given in Table S4 in Supplementary information.

The Stage I calcite grains in the SKS−TSL fault have low ΣREE+Y contents ((0.05−0.10)×10^{-6}, mean=0.07×10^{-6}). The chondrite-normalized REE patterns are flat (La_N/Yb_N=0.21−2.50, mean=1.11), with a weak positive Eu anomaly (Eu/Eu*=0.77−178, mean=1.21) and a significant negative Ce anomaly (Ce/Ce*=0.41−0.84, mean=0.56) (Fig. 12(a)). The Stage II calcite grains in the SKS−TSL fault have higher ΣREE+Y contents ((0.70−8.96)×10^{-6}, mean=3.93×10^{-6}). The LREE/HREE ratios vary from 5.70 to 12.2, with mean of 8.85, and the chondrite-normalized REE patterns are LREE-enriched (La_N/Yb_N=7.32−44.5, mean=16.2), with a significant negative Eu anomaly (Eu/Eu*=0.30−1.39, mean=0.62) and no Ce anomaly (Ce/Ce*=0.77−1.03, mean=0.93) (Figs. 12(b, c)).

The Stage I calcite grains in the CZ−LW fault have low ΣREE+Y contents ((1.07−11.06)×10^{-6}, mean=5.87×10^{-6}). Their chondrite-normalized REE patterns are also flat (La_N/Yb_N=3.11−12.7, mean=7.00), with a weak negative Eu anomaly (Eu/Eu*=0.47−1.2, mean=0.77) and a significant negative Ce anomaly (Ce/Ce*=0.01−0.06, mean=0.03) (Fig. 12(d)). The Stage II calcite grains in the outcrop of CZ−LW fault have higher ΣREE+Y contents ((0.90−24.0)×10^{-6}, mean=7.32×10^{-6}). Their chondrite-normalized REE patterns are LREE-enriched (La_N/Yb_N=4.31−189, mean=36.2), with a significant negative Eu anomaly (Eu/Eu*=0.36−0.96, mean=0.65) and no Ce anomaly (Ce/Ce*=0.76−1.13, mean=0.93) (Figs. 12(e, f)).

The Stage I calcite grains in the ZX−CCL fault also have low ΣREE+Y contents ((0.18−6.62)×10^{-6}, mean=2.35×10^{-6}) and similar REE patterns with those of SKS−TSL and CZ−LW faults (Figs. 12(g, h)). The Stage II calcite grains in the ZX−CCL fault have higher ΣREE+Y contents ((1.73−20.3)×10^{-6}, mean=7.89×10^{-6}). The LREE/HREE ratios vary from 5.03 to 15.5, with a mean value of 8.14. Their chondrite-normalized REE patterns show a decrease slope from La to Lu (La_N/Yb_N=4.85−22.6, mean=12.7), with a weak negative Eu anomaly (Eu/Eu*=0.59−0.88, mean=0.76) and no Ce anomaly (Ce/Ce*=0.86−1.07, mean=0.94) (Fig. 12(i)).

Calcite grains formed in the Stage I of the Tongshanling Cu−Pb−Zn deposit exhibit variable ΣREE+Y contents ((6.23−157)×10^{-6}, mean=60.7×10^{-6}). The LREE/HREE ratios change from 3.31 to 5.58, with a mean value of 4.16. Their chondrite-normalized REE patterns are significantly LREE-enriched, with a positive Eu anomaly (Eu/Eu*=1.24−6.52, mean=2.76) and no Ce anomaly (Ce/Ce*=0.93−1.01, mean=0.97) (Fig. 12(j)). Calcite grains formed in Stage II of the Tongshanling Cu−Pb−Zn deposit also exhibit variable ΣREE+Y contents ((19.1−119)×10^{-6}, mean=62.0×10^{-6}). Their LREE/HREE ratios range from 1.66 to 2.91, with a mean value of 2.25. Their chondrite-normalized REE patterns are significantly LREE-enriched, with a weak negative Eu anomaly (Eu/Eu*=0.71−0.93, mean=0.79) and a weak Ce negative anomaly (Ce/Ce*=0.73−0.89, mean=0.80) (Fig. 12(j)). Calcite grains formed in the Stage I and Stage II of the Weijia W deposit also exhibit variable ΣREE+Y contents ((12.3−134)×10^{-6}). Their LREE/HREE ratios range from 4.08 to 19.7. Their chondrite-normalized REE patterns are significantly LREE-enriched, with a negative Eu anomaly (Eu/Eu*=0.50−0.64) and no Ce positive anomaly (Ce/Ce*=0.90−1.04) (unpublished,

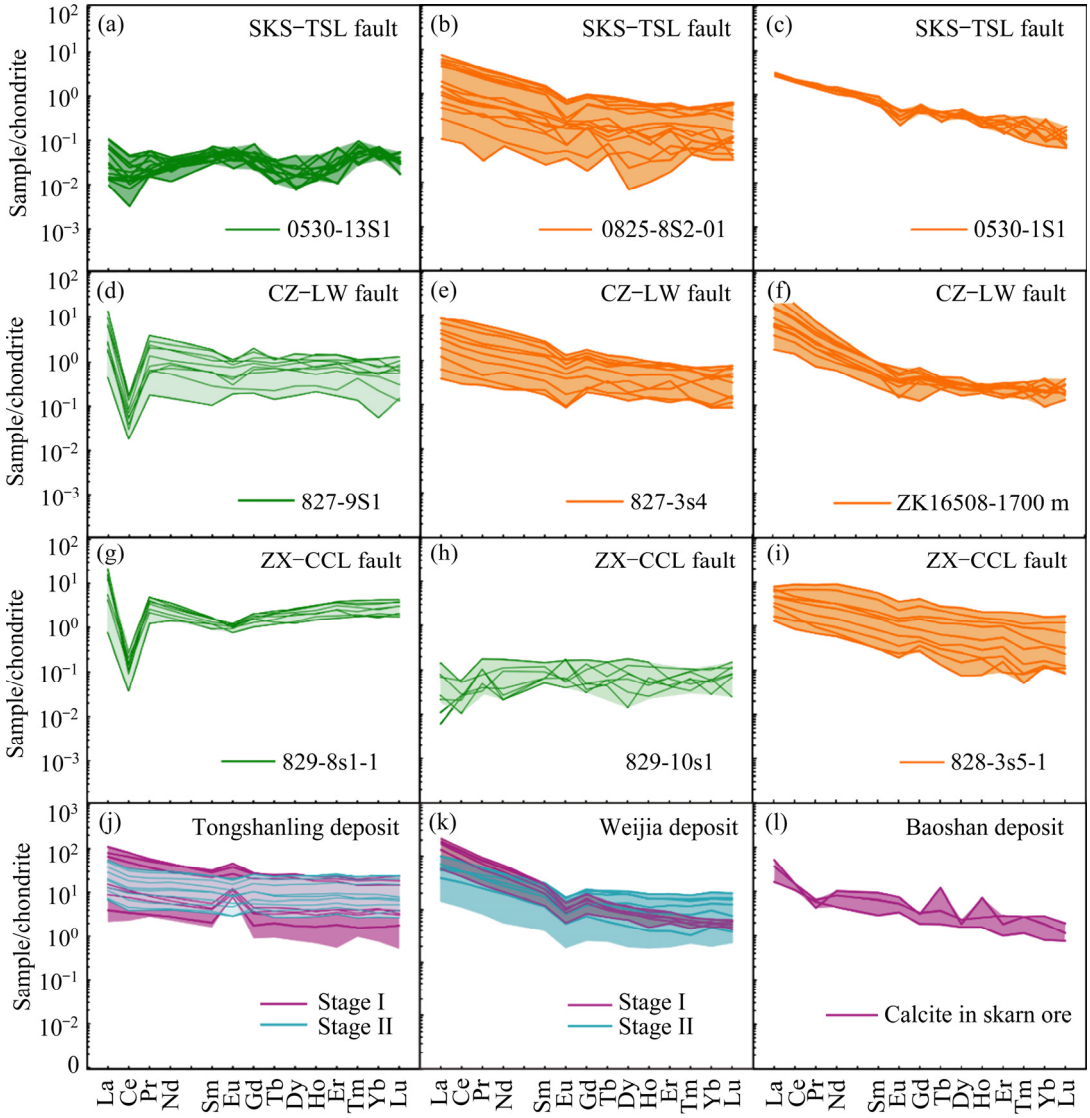

Fig. 12 Chondrite-normalized REE patterns of calcite in faults and mineral deposits in middle Qin−Hang metallogenic belt (Chondrite values are after Sun and McDonough [29]): (a−c) Two stages of calcite in SKS−TSL fault; (d−f) Two stages of calcite in CZ−LW fault; (g−i) Two stages of calcite in ZX−CCL fault; (j) Two stages of calcite in Tongshanling Cu polymetallic deposit; (k) Two stages of calcite in Weijia W deposit; (l) Calcite in Baoshan Cu polymetallic deposit [30]

Fig. 12(k)). The calcite grains formed in the skarn stage of the Baoshan Cu deposit have a similar REE pattern to that in the Tongshanling and Weijia deposits (Fig. 12(l)) [30].

The Stage I calcite grains in the SKS−TSL fault have low Fe and Mn contents (mean= 49.3×10^{-6}, 6.45×10^{-6}, respectively), and higher Sr contents ($(393-611)\times10^{-6}$, mean= 499×10^{-6}) than those of the Stage II calcite grains. The Stage I calcite grains in the CZ−LW fault have similar trends, and the Stage II calcite grains from deep drill cores have the highest Fe and Mn contents (mean=388×10^{-6}, 540×10^{-6}, respectively) and the lowest Sr contents ($(25.8-42.9)\times10^{-6}$, mean= 30.5×10^{-6}). The contents of ore-forming elements (e.g., W, Sn, Cu, Pb) are less than 1×10^{-6} in almost all samples, but the Zn contents are significantly higher than those of the Stage II calcite grains in faults ($>1\times10^{-6}$).

4.5 C−O isotopic compositions of calcite

The carbon and oxygen isotopic compositions of the Stage I and Stage II calcite grains in the faults and mineral deposits are presented in Table S5 in Supplementary information. The $\delta^{18}OH2O$ values of fluids are calculated by using the calcite−H_2O fractionation equilibrium [31]:

$$\delta^{18}OSMOW=1.03086\delta^{18}OPDB+30.86$$

The δ^{13}CPDB and δ^{18}OSMOW values of the Stage I calcite grains in the SKS−TSL, CZ−LW and ZX−CCL faults range from −4.33‰ to 1.48‰ with an average value of −1.18‰, and 17.1‰ to 21.0‰ with an average of 18.9‰, respectively. The δ^{13}CPDB and δ^{18}OSMOW values of the Stage II calcite in the SKS−TSL, CZ−LW and ZX−CCL faults range from −4.33‰ to 1.17‰ with an average of −1.62‰, and 9.78‰ to 15.5‰ with an average of 12.6‰, respectively. The δ^{18}OSMOW values of the Stage I calcite grains are slightly higher than those of the Stage II calcite grains (Fig. 13).

The δ^{13}CPDB values of calcites in the Tongshanling, Weijia, Baoshan, and Changchengling deposits range from −7.70‰ to −2.08‰ with an average of −3.76‰ and the δ^{18}OH2O values of fluid range from 10.3‰ to −15.5‰ with an average of −12.5‰, which is identical to those of Stage II calcites in the SKS−TSL, CZ−LW and ZX−CCL faults. The δ^{13}CPDB and δ^{18}OSMOW values of calcites in the limestone from the Devonian Qiziqiao formation are 1.45‰ and 20.83‰, respectively. The δ^{13}CPDB and δ^{18}OSMOW values of calcites in the limestone from the Carboniferous Shidengzi formation are 1.36‰ and 19.8‰, respectively, which is similar to the composition of marine carbonate.

5 Discussion

5.1 Polyphase tectonic events and magmatic activities

Field structural observations have identified four deformation events in the study area: D_1 is related to E−W to WNW−ESE shortening associated with the collision between the Yangtze and Cathaysia blocks; D_2 is characterized by top to the NW thrusting due to subduction of the paleo-Pacific plate; D_3 extensional deformation is accompanied by large-scale magmatic activities and W−Sn and Cu−Pb−Zn polymetallic mineralization; D_4 is a strike-slip deformation event after the mineralization.

D_1 is interpreted as a regional progressive shortening event. During D_1, a series of nearly N-trending upright and inclined folds developed in the Devonian, Carboniferous, and Permian strata that contain widespread nearly N-striking compaction cleavages (Fig. 2). In addition, some granitic dikes were intruded along the compaction cleavages and the SKS−TSL and ZX−CCL faults (Figs. 4(c), 8(a) and 10(a)), but no hydrothermal activity and Cu−Pb−Zn mineralization occurred in D_1 within the study area (Fig. 4(c)), except minor W mineralization in the Wangxianling ore field (molybdenite Re−Os age: (224.0±1.9) Ma) [33]. In the SKS−TSL fault, a granitic dyke (zircon U–Pb age: (252.8±1.1) Ma, Fig. 8(a)) was intruded into the compaction cleavages during the D_1 event [34]. The low εHf(t) values (from −10.79 to −5.87) and old T_{DMC} ages (1651−1965 Ma) further confirm that it was originated from the thickened lower crust (Fig. 11(a)). Therefore, the abnormal high-resistance body below the SKS−TSL fault may be not caused by Permian granite and is more likely the response of Jurassic granite (Fig. 7(d)). A fine-grained and muscovite-bearing granitic dyke

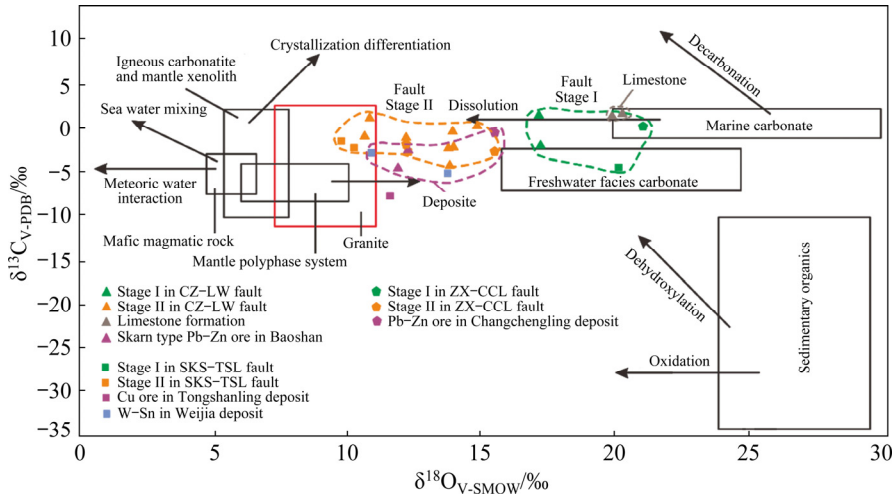

Fig. 13 $\delta^{13}C_{PDB}$−$\delta^{18}O_{SMOW}$ diagram of calcite in faults and mineral deposits within middle Qin−Hang metallogenic belt (modified from LIU et al [32])

(zircon U–Pb age: (229.3±7.6) Ma) in the Changchengling Pb–Zn deposit filled in the fault has no compressional deformation, indicating that it was intruded during the post-orogenic extension, similar to the Wangxianling and Xitian plutons [17]. Although the quartz vein type Pb–Zn orebodies are related to the fault in the shallow level (<500 m), the abnormal high-resistance body (>1 km wide) below the ZX−CCL fault may be caused by Triassic granitic plutons. Extensive Rb, Li, Nb and Ta mineralization has been discovered in the fine-grained muscovite granite pluton [35], implying that there may be a W polymetallic orebody in the contact zone of the pluton (Fig. 7(c)).

During the Permian and Triassic, closure of the Paleo-Tethyan Ocean on both sides of the South China Block and its collision caused the South China Block to be compressed and thickened. Thermal-stress relaxation will occur during the time interval of 10−20 Ma after the thickening of the crust and will result in underplating of ultrabasic−basic−alkaline magmas to form peraluminous granite [17]. Most of the Triassic granites in the Qin−Hang metallogenic belt are not mineralized, and only a small amount of rock masses is related to the W polymetallic mineralization [36], such as Limu, Wangxianling, Longshang, and Changchengling deposits [36]. In addition, all granitic intrusions related to Triassic mineralization are dated at 220−230 Ma when the tectonic setting was changed into a post-orogenic extension setting [19].

In the Early Jurassic, the study area was transformed from the Tethyan tectonic regime to the subduction regime of Paleo-Pacific plate [37]. The D_2 compressional deformation can be interpreted as the remote effects of the subduction of the Paleo-Pacific plate [34]. The D_2 structures are dominated by NNE-striking and ESE-dipping reverse faults with a dip angle of ~45° in the Changchengling, Shuikoushan and Tongshanling ore fields (Fig. 10(m)). The formation of bimodal volcanic rocks, A-type granite, and lamprophyre dykes (170−180 Ma) indicates the termination of D_2 deformation and the beginning of D_3 extension [13,34,38].

In the Middle Jurassic, the Pacific plate began to retreat or was subducted in a NE direction, and the intracontinental tectonic setting was changed from a compressional environment to an extensional environment [1]. The D_3 extensional event was resulted from the retreat of the Paleo-Pacific plate, and the lithospheric extension was caused by asthenosphere upwelling [6]. Large-scale A- or S-type granites and I-type granites (150−160 Ma) were intruded in this period and were associated with W−Sn and Cu−Pb−Zn mineralization, respectively [7]. The wide-field electromagnetic profiles reveal that the pluton emplacement is controlled by regional faults (Fig. 7). Although on the surface, some plutons are not exposed, the shallow skarn orebodies, quartz porphyry dikes and the calcite veins in the faults are probably derived from deep plutons (Figs. 4(a−i)). The U−Pb ages of zircon from a quartz porphyry dike in the SKS−TSL fault confirms that it was formed at the same time as the granitic porphyry (Figs. 10(b, d)), and their similar $\varepsilon Hf(t)$ values suggest a similar source (Figs. 11(b, d)). The D_4 deformation event is characterized by dextral strike−slip (Figs. 5(j−l)). The strike−slip movement along an irregularly shaped fault system leads to the convergence or divergence deformation at fault bends (Fig. 5(l)). The strike−slip faults crosscut the Late Jurassic granite and Cu−Pb−Zn orebodies with offset up to 300 m (Figs. 5(j−l)).

5.2 Genetic relationship of fault fluids and mineralization

5.2.1 Comparison of REE patterns of calcite

As a reaction product of hydrothermal fluid and limestone, calcite is widely developed in limestone, faults, and W−Sn and Cu−Pb−Zn deposits in the middle Qin−Hang metallogenic belt (Fig. 5). Rare earth elements are stable in the fluid migration process and the REE patterns of calcite can reveal the source and evolution of fluid [39]. The analytical results of rare earth elements show that the Stage I and Stage II calcite grains have distinct ∑REE+Y contents and REE patterns (Fig. 12). The ΣREE+Y contents of the Stage II calcite crystals are significantly higher than those of the Stage I calcite grains in the three regional faults (Table S3 in Supplementary information). Precipitation of REE-enriched minerals (e.g., garnet, scheelite and calcite) can cause variation in the ΣREE+Y contents as they capture large amounts of REE (especially HREE) in the ore-forming fluid [40], and so the ΣREE+Y contents will be gradually decreased with time.

In addition to the change in the ΣREE+Y contents, the REE patterns of calcite are also significantly different between the Stage I and Stage II (Fig. 12). The LREEs are depleted more significantly in the Stage I calcite, and their Ce anomalies are obviously different (Fig. 12). The ideal calculated radius of REE^{3+} for eight-coordination Ca^{2+} is 1.10 Å in calcite, which is quite close to that of LREEs ($^{[6]}r\ Ca^{2+}$=1.10 Å, $^{[6]}r\ La^{3+}$=1.032 Å, $^{[8]}r\ Nd^{3+}$=0.983 Å, $^{[8]}r\ Lu^{3+}$=0.861 Å) [41]. Therefore, calcite preferentially incorporates LREEs with maximum compatibility in ionic radius and the calcite precipitated from the hydrothermal system is enriched in LREEs [42]. However, it cannot explain the LREEs-depleted pattern of the Stage I calcite. A possible reason is that the Stage I fluid is depleted in LREEs. Therefore, the Stage I and Stage II calcites have different fluid sources, and the significant negative Ce anomaly of the Stage I calcite grains suggests that they may have been derived from marine limestone [43]. The LREEs-enriched REE patterns of the Stage II calcite grains in fault are similar to those of the calcite grains in the W−Sn and Cu−Pb−Zn deposits (Fig. 12) [29], which indicates that the source of the Stage II fault fluid is similar to that of the ore-forming fluid.

Elements Y and Ho have similar ionic radius, and the Y/Ho ratios are consistent in a single hydrothermal system, and therefore they can be used to reveal the source of fluid [43,44]. The Y/Ho ratios of the Stage II calcite grains in three faults range from 23.3 to 69.4, with an average value of 40.9 (Table S4 in Supplementary information), which is identical to those of calcite grains in the W−Sn and Cu−Pb−Zn deposits (27.2−61.3, mean=37.6) (Fig. 14). In the Y/Ho vs La/Ho diagram (Fig. 14), the Y/Ho and La/Lu ratios of the Stage II calcite grains in faults and W−Sn and Cu−Pb−Zn deposits are similar, which implies that they are derived from the same fluid source that may have been generated from the granitic plutons. However, the Stage I calcite in three faults has a larger range of variation in the Y/Ho ratios (6.96−106, mean=57.7) (Table S4 in Supplementary information). This suggests that the fluid source of the Stage I calcite in faults is different from that of the Stage I calcite in the W−Sn and Cu−Pb−Zn deposits.

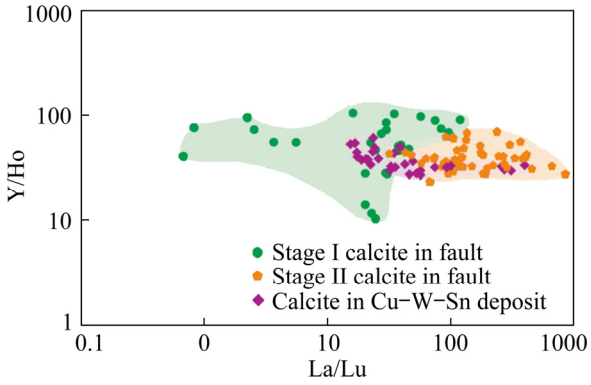

Fig. 14 Y/Ho−La/Lu plot of calcite in faults and deposits within middle Qin−Hang metallogenic belt (modified from IRBER [44])

5.2.2 Fluid source constrained by C−O isotopes

The $\delta^{13}C_{PDB}$ and $\delta^{18}O_{SMOW}$ values of the Stage II calcite grains from the three faults are plotted near the edge of the magmatic fluid field or closer to the magmatic water field, similar to those of calcite grains from the Cu−Pb−Zn deposits (Fig. 13) [45]. This indicates that the Stage II fault fluid and ore-forming fluid of the Cu−Pb−Zn mineralization was mainly originated from a magmatic hydrothermal fluid, and a small amount of wall rock materials was mixed into the ore-forming fluid in the Stage II. However, in the $\delta^{13}C_{PDB}$ vs $\delta^{18}O_{SMOW}$ diagram (Fig. 13), all data of the Stage I calcite grains are also plotted near the edge of the marine limestone field, similar to the wall rocks of the Carboniferous Shidengzi Formation and the Devonian Qiziqiao Formation. This confirms that the Stage I calcite grains with flat REE patterns are derived from limestone in the wall rocks.

In summary, although the Jurassic granite plutons have not been identified in some parts of the faults, the age of the D_3 deformation, and the REE patterns and C−O isotopic compositions of calcite grains suggest that they have a close spatial-temporal and genetic relationship with the Jurassic granite (150−160 Ma) and the W−Sn and Cu−Pb−Zn deposits.

5.3 Implication for deep exploration

Under the background of global plate collision and aggregation, the South China plate was formed in the Silurian [46] and experienced polyphase tectonic events, including the Triassic collision, the subduction and back-arc extension of the ancient

Pacific plate in the Jurassic (Fig. 15) [8,47]. Multi-stage granitoids are distributed in the middle Qin−Hang metallogenic belt, South China, and their metallogenic potential and metallogenic types are significantly different [2,6,17]. The W−Sn and Cu−Pb−Zn mineralization is closely related to granites and is mainly controlled by faults [3,4,20]. However, due to the thick cover of limestone, the alteration effect of the deep granitic plutons on the surface rocks is very small. Therefore, it is very difficult to use traditional geochemical exploration or drilling methods to explore mineral deposits in the deep level.

During the Triassic compressional deformation stage, magmatic activity was dominated by some granitic dykes or plutons, forming some small magmatic type Rb−Nb−Ta deposits and magmatic-hydrothermal type W deposits, such as the Changchengling Rb−Pb−Zn deposit and the Wangxianling W deposit (Fig. 15(a)) [35,36]. Large W–Sn and Cu–Pb–Zn deposits are mainly related to the extensional deformation during the Late Jurassic (Fig. 15(c)) [6]. The normal faults formed during this stage are steep and are connected with the deep concealed granitic intrusions (Figs. 7 and 15). In the outcrops and shallow parts of the Jurassic normal faults, multiple stages of calcite were formed, and the Stage II calcite is closely related to magmatic fluids (Figs. 5 and 6). Therefore, it is necessary to identify these normal faults for deep exploration, and to obtain the geological information of deep magmatic fluids by deciphering the mineralogical characteristics, REE patterns, and C−O isotopic compositions of calcite in the faults for understanding the W−Sn and Cu−Pb−Zn mineralization processes.

The wide-field electromagnetic profiles reveal the presence of abnormally high-resistance bodies 1−5 km below the surface normal faults with Stage II calcite (Fig. 7). 3D modelling also shows that the abnormally high-resistance bodies have an intrusive geometry that is obviously different from the sedimentary strata (Fig. 7(b)) [20]. It is suggested that the anomalies are granitic plutons because of their higher electrical resistivity than limestone [48], which is further confirmed by the drilling results of

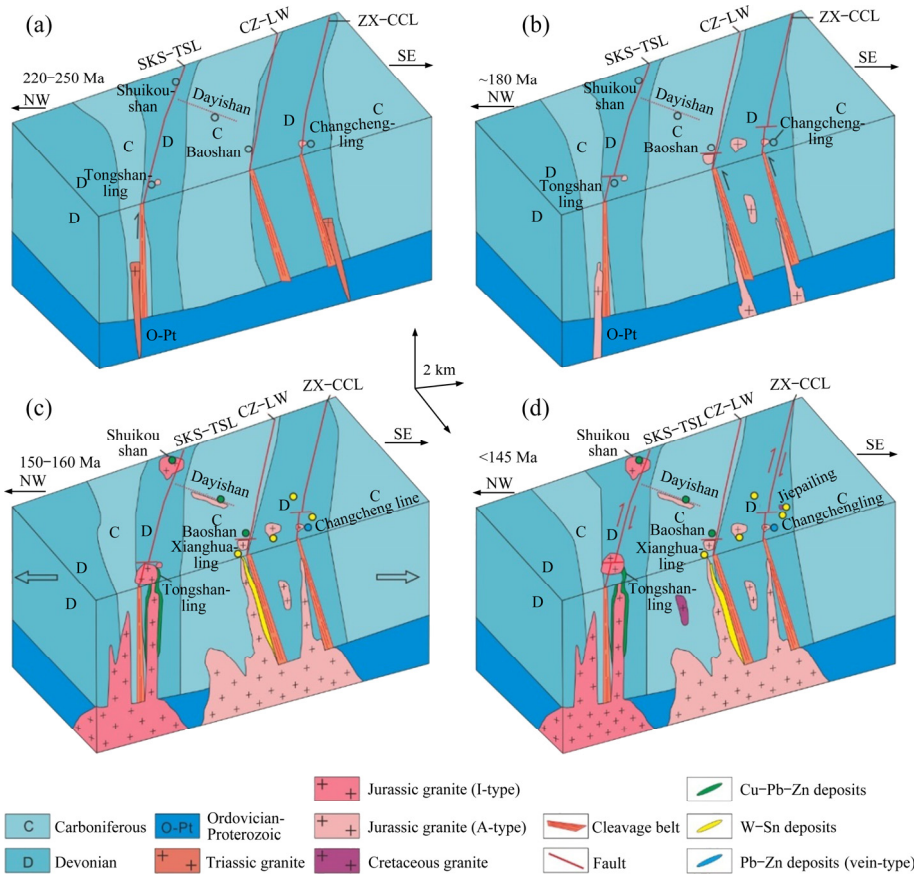

Fig. 15 Structure−magma-mineralization model for deep exploration in middle Qin−Hang metallogenic belt: (a) D_1 compressional deformation in Permian; (b) D_2 compressional deformation in Early Jurassic; (c) D_3 extensional deformation and magma-mineralization in Late Jurassic; (d) D_4 strike−slip deformation after mineralization

drill holes ZK902 and ZK1102 in the Tongshanling Cu polymetallic deposit (Fig. 7(d)). The transitional zones between the high-resistance and low-resistance bodies often correspond to the skarn type W−Sn and Cu−Pb−Zn orebodies (Figs. 7(a, d)). They are steadily extended to a depth of 3−4 km, indicating a great deep exploration potential. The regional normal faults also have a good response in the wide-field electromagnetic profiles, and they commonly appear as a low-resistance abnormal zone with a large dip angle of 60°−90° (Fig. 7). Although Pb−Zn ore and limestone have obviously different resistivities [48] and this kind of orebodies have been found in the shallow part of the Changchengling deposit, the response of quartz vein type Pb–Zn orebodies are not obvious in the wide-field electromagnetic profiles (Fig. 7(c)). This may be due to the fact that width of the orebodies is relatively small (generally less than 2 m), and can not be detected by the wide-field electromagnetic sounding, or because of the interference with shallow low-resistance bodies [20,25].

Although the morphology of the concealed granitic plutons was revealed by the wide-field electromagnetic profiles and 3D modelling, their chronological and geochemical characteristics cannot be directly determined, which hinders the prediction of the mineralization potential and identification of exact rock types [2,12]. In this study, some small granitic dikes are often developed in the shallow part of faults. They may be the branches of deep plutons and can be used to reveal detailed information about the concealed granitic plutons (Fig. 7). The zircon U−Pb dating of dikes can directly constrain the diagenetic age and the possible W−Sn and Cu−Pb−Zn mineralization age related to the dikes and plutons. For example, the Tongshanling, Baoshan and Xianghualing deposits were mainly formed in the Jurassic, while the Changchengling deposit was formed in the Triassic (Fig. 10). The zircon Hf isotopes can further reveal the source of the granitoids. For example, the granodiorite at Tongshanling is mainly derived from crustal materials, and the granite porphyry at Weijia is originated from mixing of crustal and mantle materials [17]. By combining the geochemical characteristics of intrusive rocks, granodiorite is the I-type granite, and is closely related to Cu−Pb−Zn mineralization, while granitic porphyry is the A-type granite, and is closely related to W−Sn mineralization. The lithologies of granitoids are completely consistent with the types of mineralization (e.g. Tongshanling Cu−Pb−Zn deposit and Weijia W deposit). In addition, some vein-type Pb−Zn deposits in South China are also distributed in the distal W−Sn deposits, which may be related to the A-type granite and W−Sn deposits, such as the Congshuban Pb−Zn and Shizhuyuan W−Sn deposits [49].

Therefore, the structures, magmas, and W–Sn and Cu−Pb−Zn mineralization in the shallow and deep levels are coupled in time and space, and are closely related to each other in genesis (Fig. 15). The combination of structural investigation and wide-field electromagnetic sounding provides us a new perspective for deep exploration, especially in the areas covered by thick sedimentary rocks (Fig. 7). The mineralogy, chronology and geo-chemical analyses of calcite and zircon further constrain the ore-forming fluid characteristics, source, and the possible types of mineralization (Figs. 12 and 13). Deep drilling in the Tongshanling and Baoshan Cu−Pb−Zn deposits has confirmed that this method is very effective in the middle Qin−Hang metallogenic belt, South China (Figs. 7(a, d)).

6 Conclusions

(1) Macroscopic and microscopic observations have identified four deformation events in the middle Qin−Hang metallogenic belt, South China: D_1 is a nearly E−W to WNW−ESE shortening event; D_2 is a top to the NW thrusting event; D_3 is a NW−SE-oriented extensional event; D_4 is a dextral strike–slip event related to the NE–trending faults.

(2) During the D_3 regional extensional event, large scale granite emplacement and W−Sn and Cu−Pb−Zn mineralization occurred. The similarity in REE patterns and C−O isotopic compositions of the Stage I calcite grains in the faults and the W−Sn and Cu−Pb−Zn deposits suggests that they have similar genetic mechanism and sources in response to the NW−SE regional extension during the Late Jurassic.

(3) The wide-field electromagnetic profiles reveal the deep extension (1.5−4 km) of the surface regional faults and the skarn type W−Sn and Cu−Pb−Zn orebodies. Some concealed granitic plutons are also identified to correspond with the

abnormally high-resistance bodies 1−5 km below the normal faults with Stage II calcite.

(4) The combination of structural analysis, geochemistry and wide-field electromagnetic sounding provides superior constraints on deep exploration of the W−Sn and Cu−Pb−Zn deposits related to magmatic-hydrothermal fluids, especially in the areas covered by thick sedimentary rocks in the middle Qin−Hang metallogenic belt, South China.

Supplementary information

Supplementary information in this paper can be found at: http://tnmsc.csu.edu.cn/download/18-p0254-2021-1262-Supplementary_information.pdf.

Acknowledgments

This work was financially supported by the National Key Research and Development Plan of China (Nos. 2018YFC0603903, 2018YFC0603902 and 2018YFC0603901).

References

[1] MAO Jing-wen, CHENG Yan-bo, CHEN Mao-hong, FRANCO P. Major types and time–space distribution of Mesozoic ore deposits in South China and their geodynamic settings [J]. Mineralium Deposita, 2013, 48(3): 267−294.

[2] CHEN Jun, WANG Ru-cheng, ZHU Jin-chu, LU Jian-jun, MA Dong-sheng. Multiple-aged granitoids and related tungsten-tin mineralization in the Nanling Range, South China [J]. Science China Earth Sciences, 2013, 56(12): 2045−2055.

[3] HUANG Xu-dong, LU Jian-jun. Geological characteristics and Re-Os geochronology of Tongshanling polymetallic ore field, south Hunan, China [J]. Acta Geol Sin−Engl Ed, 2014, 88: 1626−1629.

[4] DENG Xiao-dong, LUO Tao, LI Jian-wei, HU Zhao-chu. Direct dating of hydrothermal tungsten mineralization using in situ wolframite U−Pb chronology by laser ablation ICP-MS [J]. Chemical Geology, 2019, 515: 94−104.

[5] LI Jian-guo, LI Jian-kang, WANG Deng-hong, LIU Jian, HE Han-han. The deep tectonic features of Qitianling ore-concentrated area in Southern Hunan Province and its contrains to the regional ore-forming processes [J]. Acta Geologica Sinica, 2014, 88(04): 695−703. (in Chinese)

[6] ZHOU Yun, LIANG Xin-quan, WU Shi-chong, CAI Yong-feng, LIANG Xi-rong, SHAO Tong-bin, WANG Ce, FU Jian-gang, JIANG Ying. Isotopic geochemistry, zircon U−Pb ages and Hf isotopes of A-type granites from the Xitian W−Sn deposit, SE China: Constraints on petrogenesis and tectonic significance [J]. Journal of Asian Earth Sciences, 2015, 105: 122−139.

[7] WEI Wei, CHEN Yan, FAURE M, MARTELET G, LIN Wei, WANG Qing-chen, YAN Quan-ren, HOU Quan-lin. An early extensional event of the South China Block during the Late Mesozoic recorded by the emplacement of the Late Jurassic syntectonic Hengshan Composite Granitic Massif (Hunan, SE China) [J]. Tectonophysics, 2016, 672: 50−67.

[8] ZHOU Xin-min, SUN Tao, SHEN Wei-zhou, SHU Liang-shu, NIU Yao-ling. Petrogenesis of Mesozoic granitoids and volcanic rocks in South China: A response to tectonic evolution [J]. Episodes, 2006, 29(1): 26.

[9] YANG Ming-gui, MEI Yong-wen. Characteristics of geology and metallization in the Qinzhou-Hangzhou paleoplate juncture [J]. South China Geology, 1997(3): 52−59. (in Chinese)

[10] YU Jin-hai, O REILLY S Y, WANG Li-juan, GRIFFIN W L, ZHANG Ming, WANG Ru-cheng, JIANG Shao-yong, SHU Liang-shu. Where was South China in the Rodinia supercontinent?: Evidence from U−Pb geochronology and Hf isotopes of detrital zircons [J]. Precambrian Research, 2008, 164(1/2): 1−15.

[11] LI Xian-hua, LI Zheng-xiang, LI Wu-xian, WANG Yue-jun. Initiation of the Indosinian Orogeny in South China: Evidence for a Permian magmatic arc on Hainan Island [J]. The Journal of Geology, 2006, 114(3): 341−353.

[12] WANG Yue-jun, FAN Wei-ming, SUN Ming, LIANG Xin-quan, ZHANG Yan-hua, PENG Tou-ping. Geochronological, geochemical and geothermal constraints on petrogenesis of the Indosinian peraluminous granites in the South China Block: A case study in the Hunan Province [J]. Lithos, 2007, 96: 475−502.

[13] QUAN Tie-jun, KONG Hua, WANG Gao, FEI Li-dong, GUO Bi-ying, ZHAO Zhi-qiang. Petrogenesis of the Granites in the Huangshaping area: constraints from petrochemistry, zircon U-Pb chronology and Hf isotope [J]. Geotectonica et Metallogenia, 2012, 36(4): 597−606. (in Chinese)

[14] CEN Tao, LI Wu-xian, WANG Xuan-ce, PANG Chong-jin, LI Zheng-xiang, XING Guang-fu, ZHAO Xi-lin, TAO Ji-hua. Petrogenesis of early Jurassic basalts in southern Jiangxi Province, South China: Implications for the thermal state of the Mesozoic mantle beneath South China [J]. Lithos, 2016, 256: 311−330.

[15] WANG Zhi-qiang, CHEN Bin, MA Xing-hua. Petrogenesis of the Late Mesozoic Guposhan composite plutons from the Nanling Range, South China: implications for W−SN mineralization [J]. American Journal of Science, 2014, 314(1): 235−277.

[16] KONG Hua, WU Jing-hua, LI Huan, CHEN She-fa, LIU Biao, WANG Gao. Early Paleozoic tectonic evolution of the South China Block: Constraints from geochemistry and geochronology of granitoids in Hunan Province [J]. Lithos, 2021, 380: 105891.

[17] WU Qian-hong, CAO Jing-ya, KONG Hua, SHAO Yong-jun, LI Huan, XI Xiao-shuang, DENG Xuan-tong. Petrogenesis and tectonic setting of the early Mesozoic Xitian granitic pluton in the middle Qin-Hang Belt, South China: Constraints from zircon U−Pb ages and bulk-rock trace element and Sr−Nd−Pb isotopic compositions [J]. Journal of Asian Earth Sciences, 2016, 128: 130−148.

[18] HUANG Xu-dong, LU Jian-jun, SIZARET S, WANG Ru-cheng, WU Jing-wei, MA Dong-sheng. Reworked restite

enclave: Petrographic and mineralogical constraints from the Tongshanling intrusion, Nanling Range, South China [J]. Journal of Asian Earth Sciences, 2018, 166: 1−18.

[19] BAI Dao-yuan, MA Tie-qiu, WANG Xian-hui, ZHANG Xiao-yang, CHEN Bi-he. Progress in the study of Mesozoic tectono-magmatism and mineralization in the central segment of the Nanling Mountains Summary of major achievements of the 1:250, 000 geological survey in southeastern Hunan [J]. Geology in China, 2008, 35(3): 436−455. (in Chinese)

[20] JIANG Yong-fang, LI Fang-shu, CAO Yuan, XIA Ling-yun, ZHANG Ting. Discussion and research on the application of the wide field electromagnetic method to the exploration of metal ore deposits [J]. Geophysical and Geochemical Exploration, 2020, 44(5): 1073−1077. (in Chinese)

[21] SUN Hai-rui, ZHAO Zheng, YAN Guang-sheng, LV Zhi-cheng, HUANG Zhi-long, YU Xiao-fei. Geological and geochronological constraints on the formation of the Jurassic Maozaishan Sn deposit, Dayishan orefield, South China [J]. Ore Geology Reviews. 2018, 94: 212−224.

[22] YANG jie-hua, KANG Li-fang, LIU Liang, PENG Jian-tang, QI You-qiang. Tracing the origin of ore-forming fluids in the Piaotang tungsten deposit, South China: Constraints from in-situ analyses of wolframite and individual fluid inclusion [J]. Ore Geology Reviews, 2019, 111: 102939.

[23] HU Rui-zhong, BI Xian-wu, JIANG Guo-hao, CHEN Hong-wei, PENG Jian-tang, QI You-qiang, WU Li-yan, WEI Wen-feng. Mantle-derived noble gases in ore-forming fluids of the granite-related Yaogangxian tungsten deposit, Southeastern China [J]. Mineralium Deposita, 2012, 47(6): 623−632.

[24] ZHAO Zheng, WANG Deng-hong, CHEN Yu-chuan, LIU Shan-bao, FANG Gui-cong, LIANG Ting, GUO Na-xin, WANG Shao-yi, WANG Hao-yang, LIU Zhan-qing. "Jiulongnao metallogenic model" and the demonstration of deep prospecting: The extended application of "Five levels + Basement" exploration model [J]. Earth Science Frontiers, 2017, 24(5): 8−16. (in Chinese)

[25] HE Ji-shan. New research progress in theory and application of wide field electromagnetic method [J]. Geophysical and Geochemical Exploration, 2020, 44(5): 985−990. (in Chinese)

[26] GRIFFIN W L, WANG Xiang, JACKSON S E, PEARSON N J, O'REILLY S Y, XU Xi-sheng, ZHOU Xin-min. Zircon chemistry and magma mixing, SE China: In-situ analysis of Hf isotopes, Tonglu and Pingtan igneous complexes [J]. Lithos, 2002, 61: 237−269.

[27] GONFIANTINI R, STICHLER W, ROZANSKI K. Standards and intercomparison materials distributed by the International Atomic Energy Agency for stable isotope measurements [R]. Vienna, IAEA-TECDOC-825, 1995, 13−30.

[28] HOSKIN P W, SCHALTEGGER U. The composition of zircon and igneous and metamorphic petrogenesis [J]. Reviews in mineralogy and geochemistry, 2003, 53(1): 27−62.

[29] SUN Shen-su, MCDONOUGH W F. Chemical and isotopic systematics of oceanic basalts: Implications for mantle composition and processes [J]. Geological Society, London, Special Publications, 1989, 42(1): 313−345.

[30] LI Rong-qing. Rare earth element distribution and its genetic signification of calcite in Southern Hunan province [J]. Mineralogy and Petrology, 1995, 15(4): 72−77. (in Chinese)

[31] FRIEDMAN I, O'NEIL J R. Compilation of stable isotope fractionation factors of geochemical interest [R]. US Government Printing Office, 1977.

[32] LIU Jia-jun, HE Ming-qin, LI Zhi-ming, LIU Yu-ping, LI Chao-yang, ZHANG Qian, YANG Wei-guang, YANG Ai-ping. The oxygen and carbon isotopic geochemistry and its significance in Baiyangping silver copper polymetallic metallogenic concentration area, Lanping Basin [J]. Mineral Deposits, 2004, 23, 1−10. (in Chinese)

[33] ZHANG Rong-qing, LU Jian-jun, WANG Ru-cheng, YANG Ping, ZHU Jin-chu, YAO Yuan, GAO Jian-feng, LI Chao, LEI Ze-heng, ZHANG Wen-lan. Constraints of in situ zircon and cassiterite U−Pb, molybdenite Re−Os and muscovite 40Ar–39Ar ages on multiple generations of granitic magmatism and related W−Sn mineralization in the Wangxianling area, Nanling Range, South China [J]. Ore Geology Reviews, 2015, 65: 1021−1042.

[34] XU Xian-bin, ZHANG Yue-qiao, JIA Dong, SHU Liang-shu, WANG Rui-rui. Early Mesozoic geotectonic processes in South China [J]. Geology in China, 2009, 36(3): 573−593. (in Chinese)

[35] ZHU En-yi, WANG Lei, REN Tao, XIAO Qing-fei, HAN Run-sheng, XIE Xian, JIANG Zong-he, LI Yang-hai. Occurrence and regularity of ore-forming elements in the Changchengling super-large Rb−Nb−Ta deposit, Southern Hunan [J]. Journal of Central South University (Science and Technology), 2021, 52(3): 1040−1047. (in Chinese)

[36] CHEN Jun, WANG Ru-cheng, ZHU Ji-chu, LU Jian-jun, MA Dong-sheng. Tungsten tin mineralization of multi age granites in Nanling [J]. Scientia Sinica (Terrae), 2014, 44(1): 111−121. (in Chinese)

[37] ZHANG Yue-qiao, XU Xian-bin, JIA Dong, SHU Liang-shu. Deformation record of the change from Indosinian collision-related tectonic system to Yanshanian subduction-related tectonic system in South China during the early mesozoic [J]. Earth Science Frontiers, 2009, 1. (in Chinese)

[38] CHEN Pei-rong, HUA Ren-min, ZHANG Bang-tong, LU Jian-jun, FAN Chun-fang. Early Yanshanian post-orogenic granitoids in the Nanling region [J]. Science in China Series D: Earth Sciences, 2002, 45(8): 755−768.

[39] ZENG Zhi-gang, LI Chao-yang, LIU Yu-ping, TU Guang-zhi. REE geochemistry of scheelite of two genetic types from Nanyangtian, Southeastern Yunnan [J]. Geology, 1998: 26(2): 34−38.

[40] LIU Biao, LI Huan, WU Qian-hong, EVANS N J, CAO Jing-ya, JIANG Jiang-bo, WU Jing-hua. Fluid evolution of Triassic and Jurassic W mineralization in the Xitian ore field, South China: Constraints from scheelite geochemistry and micro thermometry [J]. Lithos, 2019, 330: 1−15.

[41] SHANNON R D. Revised effective ionic radii and systematic studies of interatomic distances in halides and chalcogenides [J]. Acta Crystallographica Section A: Crystal Physics, Diffraction, Theoretical and General Crystallography, 1976, 32(5): 751−767.

[42] RIMSTIDT J D, BALOG A, WEBB J. Distribution of trace elements between carbonate minerals and aqueous solutions [J]. Geochimica et Cosmochimica Acta, 1998, 62(11): 1851−1863.
[43] BAU M, KOSCHINSKY A, DULSKI P, HEIN J R. Comparison of the partitioning behaviours of yttrium, rare earth elements, and titanium between hydrogenetic marine ferromanganese crusts and seawater [J]. Geochimica et Cosmochimica Acta, 1996, 60(10): 1709−1725.
[44] IRBER W. The lanthanide tetrad effect and its correlation with K/Rb, Eu/Eu∗, Sr/Eu, Y/Ho, and Zr/Hf of evolving peraluminous granite suites [J]. Geochimica et Cosmochimica Acta, 1999, 63(3/4): 489−508.
[45] POULIN R S, KONTAK D J, MCDONALD A, MCCLENAGHAN M B. Assessing scheelite as an ore-deposit discriminator using its trace-element and REE chemistry [J]. The Canadian Mineralogist, 2018, 56(3): 265−302.
[46] SHU Liang-shu. An analysis of principal features of tectonic evolution in South China Block [J]. Geological Bulletin of China, 2012, 31(7): 1035−1053. (in Chinese)
[47] WANG Yue-jun, FAN Wei-ming, LIANG Xin-quan, PENG Tou-ping, SHI Yu-ruo. Elemental and Sr−Nd isotopic systematics of the early Mesozoic volcanic sequence in southern Jiangxi Province, South China: Petrogenesis and tectonic implications [J]. International Journal of Earth Sciences, 2005, 94(1): 53−65. (in Chinese)
[48] QU Li-jun, WANG Qing, LI Bo, YAO Wei. The application of multiple geophysical methods to the study of deep metallogenic regularity in the Sanhexu mining area, the Xianghualing orefield, Hunan Province [J]. Geophysical and Geochemical Exploration, 2020, 44(6): 1313−1321. (in Chinese)
[49] ZHAO Pan-lao, YUAN Shun-da, MAO Jing-wen, YUAN Ya-bin, ZHAO Hai-jie, ZHANG Dong-liang, SHUANG Yan. Constraints on the timing and genetic link of the large-scale accumulation of proximal W−Sn−Mo−Bi and distal Pb−Zn−Ag mineralization of the world-class Dongpo orefield, Nanling Range, South China [J]. Ore Geology Reviews, 2018, 95: 1140−1160.

钦杭成矿带中段钨锡与铜多金属矿床的深部探测

戴前伟，段 旦，刘 飚，吴堑虹，严家斌，孔 华，陈社发，宗 琦，汤钰御

中南大学 地球科学与信息物理学院 有色金属成矿预测与地质环境监测教育部重点实验室，长沙 410083

摘 要：联合使用野外与显微构造调查、断层中方解石微量元素与 C−O 同位素分析、岩脉中锆石 U−Pb 定年与广域电磁测深来重建钦杭成矿带中段构造−岩浆成矿的时空演化过程与揭示其成因联系。研究结果表明，存在 4 期构造变形事件：D_1 变形为东西向挤压，D_2 变形为从 SE 向 NW 的逆冲，D_3 变形为 NW 到 SE 的伸展事件，伴随着大规模的花岗岩体侵位以及与之有关的钨锡与铜铅锌成矿，D_4 变形为成矿后的右型走滑。另外，在野外露头与深部钻孔中发现两期方解石，第二期稀土配分型式主要为 LREE 富集型，具有低的 $\delta^{18}O_{SMOW}$ 值(9.78‰~12.3‰)，与矿床中方解石的稀土配分型式一致，证实断层中第二期方解石与钨锡和铜铅锌成矿关系密切。广域电磁剖面进一步揭示~5 km 深度的构造−岩浆岩矿床的几何学特征，花岗岩体的区域断层侵入。推测浅部的钨锡与铜铅锌矿体往深部(1.5~4 km)具有稳定的延深。因此，地表调查、地球化学分析与广域电磁测深结合的方法在覆盖区对钨锡与铜铅锌矿床的深部探测十分有效。

关键词：断层；花岗岩体；方解石；稀土模式；广域电磁测深

(Edited by Bing YANG)